

1 **Observations of seasonal and diurnal glacier velocities at Mount** 2 **Rainier, Washington using terrestrial radar interferometry**

3 **K. E. Allstadt^{1*}, D.E. Shean^{1, 2}, A. Campbell¹, M. Fahnestock³, S. D. Malone¹**

4 [1]{University of Washington, Department of Earth and Space Sciences}

5 [2]{University of Washington, Applied Physics Lab Polar Science Center}

6 [3]{University of Alaska Fairbanks, Geophysical Institute}

7 [*]{now at: USGS Geologic Hazards Science Center}

8 Correspondence to: K. E. Allstadt (allstadt@uw.edu)

9 **Abstract**

10 We present surface velocity maps derived from repeat terrestrial radar interferometry (TRI)
11 measurements, and use these time series to examine seasonal and diurnal dynamics of alpine
12 glaciers at Mount Rainier, Washington. We show that the Nisqually and Emmons glaciers have
13 small slope-parallel velocities near the summit (<0.2 m/day), high velocities over their upper and
14 central regions (1.0-1.5 m/day), and stagnant debris-covered regions near the terminus (<0.05
15 m/day). Velocity uncertainties are as low as ± 0.02 - 0.08 m/day. We document a large seasonal
16 velocity decrease of 0.2-0.7 m/day (-25 to -50%) from July to November for most of the
17 Nisqually glacier, excluding the icefall, suggesting significant seasonal subglacial water storage
18 under most of the glacier. We did not detect diurnal variability above the noise level. Simple 2D
19 ice flow modeling using TRI velocities suggests that sliding accounts for 91% and 99% of the
20 July velocity field for the Emmons and Nisqually glaciers with possible ranges of 60 - 97% and
21 93 - 99.5%, respectively, when considering model uncertainty. We validate our observations
22 against recent in situ velocity measurements and examine the long-term evolution of Nisqually
23 glacier dynamics through comparisons with historical velocity data. This study shows that repeat
24 TRI measurements with >10 km range can be used to investigate spatial and temporal variability
25 of alpine glacier dynamics over large areas, including hazardous and inaccessible areas.

26 **1 Introduction**

27 Direct observations of alpine glacier velocity can help improve our understanding of ice
28 dynamics. Alpine glacier surface velocities are typically dominated by basal sliding, which is
29 tightly coupled to subglacial hydrology (Anderson et al., 2014; Bartholomaeus et al. 2008).
30 However, the spatial extent and spatial/temporal resolution of direct velocity measurements are
31 often limited to short campaigns with sparse point measurements in accessible regions (e.g.
32 Hodge, 1974; Driedger and Kennard, 1986). Remote sensing can help overcome many of these
33 limitations. Radar interferometry, a form of active remote sensing, detects mm- to cm- scale
34 displacements between successive images of the same scene and can see through clouds and fog.
35 In the past few decades, satellite interferometric synthetic aperture radar, or InSAR (e.g.
36 Massonnet and Feigl, 1998; Burgmann et al., 2000) has emerged as an invaluable tool for
37 quantifying glacier dynamics (e.g., Joughin et al, 2010). However, limited data availability and
38 revisit times limit the application of InSAR for the study of many short-term processes.

39 Terrestrial radar interferometry (TRI), also referred to as ground-based radar interferometry, has
40 recently emerged as a powerful technique for observing glacier displacement that is not prone to
41 the same limitations (Caduff et al., 2014). Sets of radar data acquired at intervals as short as ~1
42 minute from up to several km away allow for observations of velocity changes over short
43 timescales and large spatial extents. Stacking these large numbers of interferogram pairs over
44 longer timescales can significantly reduce noise. Here, we employ this relatively new technique
45 to provide spatially- and temporally-continuous surface velocity observations for several glaciers
46 at Mount Rainier volcano in Washington State (Fig. 1). Though Rainier's glaciers are among the
47 best-studied alpine glaciers in the U.S. (Heliker et al., 1984; Nylén, 2004), there are many open
48 questions about diurnal and seasonal dynamics that TRI can help address. Specifically, many
49 aspects of subglacial hydrology and its effects on basal sliding are poorly constrained, especially
50 for inaccessible locations like the Nisqually icefall and ice cliff. Our observations provide new
51 insight into these processes through analysis of the relative magnitude and spatial patterns of
52 surface velocity over diurnal and seasonal timescales. To our knowledge, no other studies have
53 investigated seasonal changes to glacier dynamics using TRI.

54 Mount Rainier offers an excellent setting for TRI, with several accessible viewpoints offering a
55 near-continuous view with ideal line-of-sight vectors for multiple glaciers, and well-distributed

56 static bedrock exposures for calibration. The ability to image the velocity field of entire glaciers
57 from one viewpoint with minimal shadowing sets this study area apart. Most previous studies
58 only image part of the glaciers under investigation, usually due to less favorable viewing
59 geometries (e.g. Noferini et al., 2009; Voytenko et al., 2015; Riesen et al., 2011). However, the
60 steep topography and local climatic factors at Mount Rainier result in strong atmospheric
61 variability and turbulence – a major source of noise for radar interferometry techniques
62 (Goldstein, 1995). Atmospheric noise is a particular issue for the long ranges (>10 km)
63 associated with accessible viewpoints at Mount Rainier. To overcome this limitation, we
64 successfully combine, expand on, and evaluate noise reduction techniques such as stacking
65 interferograms (e.g. Voytenko et al. 2015) and deriving atmospheric noise corrections over static
66 control surfaces (bedrock exposures) (e.g. Noferini et al. 2009). We demonstrate that these
67 techniques offer significant uncertainty reductions using a novel bootstrapping approach.

68 In the following sections, we provide background on Mount Rainier’s glaciers, and detail our
69 sampling methodology and data processing techniques. We then present TRI results
70 documenting seasonal and diurnal velocity variations for the Nisqually, Wilson, and Emmons
71 Glaciers, and quantify measurement uncertainty. Next we examine the partitioning of observed
72 surface velocities between deformation and basal sliding at different times of year using a simple
73 2D flow model, and compare our observations to other recent and historical velocity
74 measurements. These comparisons provide ground truth for TRI measurements and new insight
75 into the evolution of the Nisqually glacier since the late 1960s.

76 **2 Study area**

77 With a summit elevation of 4392 m, Mount Rainier (Fig. 1) is the largest stratovolcano in the
78 Cascades and is considered the most dangerous volcano in the United States (Swanson et al.,
79 1992). It also holds the largest concentration of glacial ice in the mainland United States
80 (Driedger and Kennard, 1986) - 87 km² was covered with perennial snow and ice in 2008 (Sisson
81 et al., 2011). The steep upper sections of the major glaciers are relatively thin, with typical
82 thicknesses of ~30 to 80 m (Driedger and Kennard, 1986). Thickness increases at lower
83 elevations, with a maximum of ~200 m for the Carbon glacier, although these estimates likely
84 provide an upper bound, as these glaciers have experienced significant thinning in recent
85 decades, losing 14% of their volume between 1970 and 2008 (Sisson et al., 2011). Mass balance

86 stake measurements from 2003-2010 show that the average winter balance for Nisqually was 2.4
87 m water equivalent (m.w.e.), average summer balance was -3.5 m.w.e., and cumulative net
88 balance was -8.6 m.w.e. from 2003-2011 (Riedel, 2010; Riedel and Larrabee, 2015).

89 The glaciers of Mt. Rainier have been of interest to geoscientists for over 150 years and have a
90 long record of scientific observation (Heliker, 1984). In this study, we focus on large, accessible,
91 well-documented glaciers in the park: the Nisqually and Wilson glaciers on the southern flank,
92 and Emmons and Upper Winthrop glaciers on the northeastern flank (Fig. 1).

93 The Nisqually Glacier is visible from several viewpoints near the Paradise Visitor Center, which
94 is accessible year-round. The terminus location has been measured annually since 1918, and
95 three transverse surface elevation profiles have been measured nearly every year since 1931
96 (Heliker, 1984). Veatch (1969) documented a 24-year history of Nisqually's advances and
97 retreats and other dynamic changes through a meticulous photographic survey from 1941-1965.
98 Hodge (1974) conducted a detailed 2-year field study of the seasonal velocity cycle for the lower
99 Nisqually. He found that velocities varied seasonally by about 50%, with maximum velocities in
100 the spring (June) and minimum in the fall (November). This finding, and the lack of correlation
101 between runoff and sliding speeds, advanced the idea that efficient conduits close as meltwater
102 input decreases in the fall, leading to distributed subglacial storage through the fall, winter and
103 spring. Increased surface melting in spring and summer leads to increased subglacial discharge
104 and the opening of a more efficient network of conduits capable of releasing some of this stored
105 water (Hodge, 1974). More recently, Walkup et al. (2013) tracked the movements of supraglacial
106 rocks with high precision from 2011-2012, yielding velocity vectors for a wide network of points
107 over the lower parts of Nisqually glacier.

108 The Emmons glacier, visible from the Sunrise Visitors Center, has received less attention than
109 Nisqually, despite the fact that it is the largest glacier by area on the mountain (Driedger and
110 Kennard, 1986), mainly because it is not as easily accessible as Nisqually. A large rock fall
111 ($\sim 1.1 \times 10^7 \text{ m}^3$) from Little Tahoma in December 1963 covered much of the lower Emmons
112 glacier with a thick debris layer (Crandell and Fahnestock, 1965). The insulating debris cover
113 likely contributed to the advance and thickening of the Emmons Glacier from 1970-2008, while
114 all other glaciers on Mount Rainier experienced significant thinning (Sisson et al., 2011).
115 Average 2003-2010 winter balance for Emmons was 2.3 m.w.e., average summer balance was -

116 3.2 m.w.e , and cumulative net balance was -7.7 m.w.e. from 2003-2011 (Riedel, 2010; Riedel
117 and Larrabee, 2015).

118 The National Park Service's long-term monitoring protocols include both the Nisqually and
119 Emmons glaciers and involve regular photographs, annual mass balance measurements,
120 meltwater discharge rates, plus area and volume change estimates every decade (Riedel, 2010;
121 Riedel and Larrabee, 2015).

122 **3 Methods**

123 **3.1 Instrument description**

124 For this study, we used a GAMMA portable radar interferometer (GPRI) (Werner et al., 2008;
125 Werner et al., 2012) - a ground-based, frequency-modulated continuous waveform (FMCW)
126 radar that can capture mm-scale surface displacements. The instrument includes three 2-m
127 antennas mounted on a vertical truss, with one transmit antenna 35 cm above the upper of two
128 receiving antennas, spaced 25 cm apart (Fig. 2). The transmit antenna produces a 35° vertical
129 beam with 0.4° width that azimuthally sweeps across the scene to build a 2D radar image as the
130 truss rotates. The radar operates at a center frequency of 17.2 GHz, with selectable chirp length
131 of 2-8 ms and bandwidth of 25 to 200 MHz. The radar wavelength is 17.6 mm with range
132 resolution of ~0.75 cm and one-way interferometric change sensitivity of 8.7 mm/cycle of phase
133 providing <1 mm line-of-sight precision. Line-of-sight interferograms are generated by
134 comparing phase differences in successive acquisitions from the same viewpoint. The interval
135 between acquisitions can be as short as ~1 min, allowing for high coherence even in rapidly
136 changing scenes.

137 **3.2 Survey Description**

138 We performed four data collection campaigns in 2012 (Table 1). The first campaign occurred on
139 6-7 July 2012. This timing corresponds to just after the expected peak seasonal glacier velocities
140 at Mount Rainier (Hodge, 1974). Following the success of this study, three subsequent
141 deployments were performed during the late fall and early winter, which should capture near-
142 minimum seasonal velocity (Hodge, 1974). These campaigns were timed to occur before,
143 immediately after, and a few weeks after the first heavy snowfall of the season (2 Nov 2012, 27
144 Nov 2012 and 10 Dec 2012, respectively).

145 Three viewpoints were selected for data collection: GLPEEK and ROI, which overlook the
146 Nisqually and Wilson glaciers, and SUNRIZ, which overlooks the Emmons and upper Winthrop
147 glaciers (Fig. 1). ROI and SUNRIZ were directly accessible from park roads, which greatly
148 facilitated instrument deployment, and GLPEEK was accessed on foot. ROI was occupied
149 during all campaigns, while SUNRIZ and GLPEEK were only occupied during the July 2012
150 campaign because of access limitations. Figures A1-A3 show the field of view from each
151 viewpoint.

152 Distances from the GPRI to the summit were 6.7, 7.6, and 10.8 km from GLPEEK, ROI and
153 SUNRIZ, respectively. Radar images were continuously collected with a 3-minute interval for all
154 surveys. Total acquisition time at each site was dictated by logistics (weather conditions,
155 personnel), with ~24 hour acquisitions at SUNRIZ and ROI to capture diurnal variability.

156 The instrument was deployed on packed snow during the 6 July 2012 GLPEEK and 27 Nov and
157 10 Dec 2012 ROI acquisitions. Over the course of the GLPEEK survey, we noted limited snow
158 compaction and melt beneath the GPRI tripod with total displacement of ~2-4 cm over ~6 hours.
159 However, this instrument motion proved to be negligible for the interferogram interval used (6
160 min). We did not note significant snow compaction under the tripod during the fall/winter
161 surveys.

162 Weather conditions during the July 2012 surveys were clear with light/variable wind. The 2 Nov
163 2012 survey involved high-altitude clouds, passing showers and brief interruptions in data
164 collection. Weather conditions were clear with sun for the 27 Nov 2012 campaign, and fog with
165 limited visibility on 10 Dec 2012.

166 **3.3 Data Processing**

167 All radar data were processed with the GAMMA SAR and Interferometry software suite.
168 Interferograms were generated from single-look complex SLC products with a time separation of
169 6 minutes, though sometimes longer if acquisition was interrupted. For example images see Fig.
170 A4. Interferograms were multi-looked by 15 samples in the range direction to reduce noise. A
171 correlation threshold filter of 0.7 and an adaptive bandpass filter (ADF) with default GAMMA
172 parameters were applied to the interferograms to improve phase unwrapping. Phase unwrapping

173 was initiated in areas with high correlation scores and negligible deformation, such as exposed
174 bedrock or stagnant ice.

175 **3.3.1 Atmospheric noise corrections**

176 Slight changes in the dielectric properties of the atmosphere between the GPRI and target
177 surfaces can lead to uncertainty in the interferometric displacement measurements (Zebker et al.
178 1997; Werner et al., 2008). Changes in atmospheric humidity, temperature, and pressure can all
179 affect radar propagation velocity (Goldstein, 1995). These variations are manifested as phase
180 offsets in the received radar signal, which must be isolated from phase offsets related to true
181 surface displacements.

182 This atmospheric noise proved to be significant for the long range (i.e., ~22 km two-way
183 horizontal path at SUNRIZ), mountainous terrain (i.e., ~2.4 km vertical path from SUNRIZ to
184 summit), and turbulent atmosphere involved with this study, with the magnitude of this noise
185 often exceeding that of surface displacement signals. The scale of the atmospheric noise features
186 we observed in the data was typically much wider than the width of the glaciers, so in order to
187 minimize this atmospheric noise in the individual interferograms, we interpolated apparent
188 displacement values over static control surfaces (e.g. exposed bedrock). To do this, we fit a
189 surface using Delaney triangulation to a subset (5%) of pixels over exposed bedrock. The subset
190 of pixels was resampled randomly for each unwrapped interferogram and the interpolated result
191 was smoothed to reduce artifacts and then subtracted from the interferogram. The corrections
192 were applied to all individual interferograms, and the resulting products were stacked to further
193 reduce noise. To stack, we took all the images for a given time period and computed the mean
194 and median at each pixel. This has the effect of augmenting signal and canceling out noise. The
195 median is less affected by outliers and is our preferred result. The median line-of-sight (LOS)
196 velocities from this stack provide a single measurement with a high signal to noise ratio for the
197 entire sampling period.

198 In addition to computing the median LOS velocities for the entirety of each sampling period, we
199 also computed a running mean of the LOS velocities to characterize any short-term velocity
200 variations in the extended occupation datasets: 7-8 July SUNRIZ (24 hours) and 1-2 November
201 ROI (21 hours). The running mean was computed every 0.3 hours with a 2-hour centered
202 (acausal) window, with standard error used to estimate uncertainty.

203 Interferograms with significant phase unwrapping errors, low correlation, or anomalous noise
204 were excluded from stacking. We only excluded a few images for each site with the exception of
205 SUNRIZ, which produced many images with anomalous noise and unwrapping errors, possibly
206 due to instrument noise and/or the extended range through significant atmospheric disturbance.
207 For this reason, more than half of the data from SUNRIZ was excluded from the analysis (Table
208 2). For GLPEEK and ROI, interferograms with occasional localized unwrapping errors were
209 preserved during stacking, as they have little influence on the final stack median. However,
210 localized areas with persistent unwrapping errors in the SUNRIZ data were masked using a
211 threshold standard deviation filter of 0.6 m/day.

212 We estimated median LOS velocity uncertainties using a bootstrapping approach (Efron, 1979).
213 This involved resampling the set of images used in the stack with replacement 1000 times for
214 each campaign. Then, for each pixel, the 25th and the 975th ordered values were set as the lower
215 and upper bounds of the 95% confidence interval.

216 **3.3.2 Conversion from radar coordinates to map coordinates**

217 We developed a sensor model and tools to terrain-correct the stacked GPRI data (in original
218 azimuth, range coordinates) using an existing 2 m/pixel airborne LiDAR digital elevation model
219 (DEM) acquired in September 2007/2008 (Robinson et al., 2010). While some elevation change
220 has undoubtedly occurred for glacier surfaces between September 2008 and July 2012, the
221 magnitude of these changes (<20 m) is negligible for orthorectification purposes given the GPRI
222 acquisition geometry. A single control point identified over exposed bedrock in the LiDAR DEM
223 and the multi-look image (mli) radar data was used to constrain absolute azimuth orientation
224 information for each campaign. A ~10 m/pixel (mean of azimuth and range sample size) grid in
225 UTM 10N (EPSG: 32610) was created for each campaign, with extent computed from the GPRI
226 GPS coordinates, min/max range values, and min/max absolute azimuth values. Each 3D pixel
227 in this grid was then populated by extracting the radar sample with corresponding range and
228 azimuth.

229 **3.3.3 Correction to slope-parallel velocities**

230 While the line-of-sight vectors for these surveys are roughly aligned with surface displacement
231 vectors (median incidence angles for glacier surfaces are ~22° for GLPEEK, ~25° for SUNRIZ

232 and $\sim 26^\circ$ for ROI), glaciological analyses typically require horizontal and vertical velocity
233 components relative to the glacier surface. As each GPRI survey offers only a single look
234 direction, this is not possible. However, we can assume that displacement is dominated by
235 surface-parallel flow, and use the 2007/2008 LiDAR DEM to extract surface slopes needed to
236 estimate 3D displacement vectors (e.g., Joughin et al., 1998).

237 This approach is intended for relatively smooth, continuous surface slopes over length scales $>2-$
238 $3x$ ice thickness. It is therefore possible that the slope-parallel correction can overestimate
239 velocity for steep, high relief surfaces with significant high-frequency topographic variability
240 (e.g. icefalls). The slope-parallel assumption also begins to break down where the vertical flow
241 velocity component becomes significant. This is expected in the upper accumulation and lower
242 ablation zones, where the submergence and emergence velocities become more significant,
243 respectively, but is less important near the equilibrium-line altitude (ELA) or locations where
244 sliding dominates surface motion. The latter is expected for much of the Nisqually Glacier at
245 least (Hodge, 1974).

246 We implement a slope-parallel correction by first downsampling the 2007/2008 LiDAR DEM to
247 20 m/pixel and smoothing with a 15×15 pixel (~ 300 m), 5-sigma Gaussian filter. The slope-
248 parallel velocity (V_{sp}) is defined as:

$$249 \quad V_{sp} = V_{LOS} / (\hat{S} \cdot \hat{L}) \quad (1)$$

250 where $\hat{S} \cdot \hat{L}$ is the dot product between the unit vector pointing directly downslope from each
251 grid cell (\hat{S}) and the unit vector pointing from each grid cell to the sensor (\hat{L}). Regions where
252 the angle between these two vectors exceeded 80° were masked to avoid dividing by numbers
253 close to zero which could amplify noise.

254 **3.4 2-D glacier deformation modeling**

255 Surface flow velocity can be partitioned into internal deformation and basal sliding components.
256 We present a simple, 2-D plane-strain ice deformation model for a preliminary assessment of the
257 importance of basal sliding for the glaciers in our study area. The deformation model uses the
258 shallow ice approximation (SIA) – an approximate solution of the Stokes Equations (Greve and
259 Blatter, 2009; Cuffey and Paterson, 2010). The expected surface velocity u_s due to internal
260 deformation from the SIA model is:

261
$$u_s = \frac{2 A(\sin(\alpha)\rho_i g)^n H^{n+1}}{n+1} \quad (2)$$

262 where ρ_i represents ice density, g represents gravitational acceleration, α represents local surface
 263 slope, H represents local ice thickness, A represents an ice softness parameter and n represents a
 264 flow rate exponent. The coordinate system is vertically aligned.

265 The SIA is not well-suited for narrow mountain glaciers, so we modify it to simulate the effect of
 266 non-local conditions, such as lateral sidewall drag and longitudinal stretching. The ice thickness
 267 H and surface slope α are smoothed using a weighting function based on Kamb and Echelmeyer
 268 (1986). Kamb and Echelmeyer (1986) calculated a longitudinal coupling length l using a 1-D
 269 force balance approach, for each point in their domain. They calculated l to be in the range of
 270 one-to-three ice thicknesses for valley glaciers. We simplified this by using a single value for l
 271 over the domain of model. The longitudinal couple length l is used in a weighting function to
 272 smooth α and H . The weighting function has the form:

273
$$W(x, y) = e^{-\frac{\sqrt{(x-x')^2+(y-y')^2}}{l}} \quad (3)$$

274 where x and y represent the horizontal coordinates of the weight position, and x' and y' represent
 275 the horizontal coordinates of the reference position. Weights are calculated at each point in the
 276 model domain, over a square reference window (side length of A_w). H and α are smoothed at the
 277 reference position by normalizing weights over the reference window. We choose a coupling
 278 length l of ~ 1.5 ice thickness and an averaging window size of ~ 3 ice thicknesses, consistent
 279 with the usage in Kamb and Echelmeyer (1986). We use a spatially uniform and temporally
 280 constant ice softness parameter suitable for ice at the pressure melting point of $2.4 \times 10^{-24} \text{ Pa}^{-3} \text{ s}^{-1}$
 281 (Cuffey and Paterson, 2010, pg. 75). Ice softness can be affected by several factors (e.g.,
 282 englacial water content and impurities), so we also consider an ice softness parameter up to twice
 283 this best estimate in accounting for model uncertainties, as described below. Our best estimates
 284 of model input parameters are summarized in Table 3.

285 Surface slope (Fig. A1B) was estimated from the 2007/2008 LiDAR DEM (Robinson et al.
 286 2010). Surface velocities u_s are the TRI-derived median slope-parallel velocities. Ice thicknesses
 287 H (Fig. A1A) were estimated by differencing the 2007/2008 LiDAR DEM surface elevations and
 288 the digitized and interpolated bed topography from Driedger and Kennard (1986). The Driedger

289 and Kennard (1986) bed topography contours were derived from ice-penetrating radar point
290 measurements and surface contours from aerial photographs. The published basal contours for
291 Nisqually/Wilson, Emmons, and Winthrop Glaciers were digitized and interpolated to produce a
292 gridded bed surface using the ArcGIS Topo to Raster utility. The gridded bed elevations have
293 root mean squared error (RMSE) of 11 m when compared with the 57 original radar point
294 measurements. A point-to-plane iterative closest point algorithm (implemented in the NASA
295 Ames Stereo Pipeline `pc_align` utility (Shean et al., 2015)) was used to coregister the 1986 bed
296 topography to the 2007/2008 LiDAR topography over exposed bedrock on valley walls. Mean
297 error over these surfaces was 7.6 m following coregistration, although some of this error can be
298 attributed to actual surface evolution near glacier margins (e.g., hillslope processes) from 1986-
299 2008. In addition to these interpolation and coregistration errors, there were likely small changes
300 in ice thickness during the 4-5 years between the 2007/2008 DEM data collection and the 2012
301 TRI observations, as mass balance measurements suggest that both the Nisqually and Emmons
302 Glaciers experienced net mass loss during this time period (Riedel and Larrabee, 2015).
303 Propagation of these uncertainties results in estimated ice thickness uncertainties of ~5-25%. In
304 order to account for this large uncertainty, we ran the model with $\pm 25\%$ ice thickness as well as
305 2x ice softness in order to estimate the possible range of expected deformation velocities.

306 More sophisticated ice flow models (e.g. Gagliardini et al., 2013; Le Meur et al., 2004; Zwinger
307 et al., 2007) could potentially offer a more realistic picture of the spatial and temporal variability
308 of glacier sliding. However, given the poorly-constrained model inputs and observational
309 emphasis for this study, we proceed with the SIA model to obtain approximate estimates for the
310 deformation and sliding components of observed velocities.

311 **4 Results**

312 The median stacks of surface-parallel velocity for all viewpoints and their respective uncertainty
313 estimates are shown in Fig. 3-6. Overall, our results show that repeat TRI measurements can be
314 used to document spatial and temporal variability of alpine glacier dynamics over large areas
315 from >10 km away. The atmospheric noise removal approach was successful in extracting a
316 glacier displacement signal for all campaigns, with excellent results for Nisqually Glacier due to
317 the shorter range from ROI and GLPEEK viewpoints and limited glacier width between control
318 surfaces. Stacking alone was very effective; the velocities of the mean and median stacks with

319 and without the atmospheric noise correction were very similar. The main benefit of the extra
320 step of using stable rock points to subtract an estimate of the atmospheric noise was to
321 significantly reduce the uncertainties and to reduce the noise where velocities are slow. The
322 uncertainties before and after atmospheric correction are compared on Table 2. The median
323 width of the 95% confidence interval for each corrected, stacked pixel is plotted in Fig. 3B and
324 Fig. 5. Note near-zero values over exposed bedrock surfaces used to derive atmospheric noise
325 correction. We were able to reduce uncertainties (half the median confidence interval width) to
326 about ± 0.02 to ± 0.08 m/day over glacier surfaces for some campaigns, with uncertainty
327 dependent on the total number of stacked images, weather conditions, and target range (Table 2).
328 For example, the 6 July 2012 ROI survey had a final confidence interval width of 0.11 m/day
329 ($\sim \pm 0.06$ m/day) while the 10 Dec 2012 ROI survey had a final confidence interval width of 0.15
330 m/day ($\sim \pm 0.08$ m/day) despite a 50% increase in stack count. This is likely due to increased local
331 atmospheric variability, as low-altitude clouds obscured the surface during 10 Dec 2012 survey.
332 The 2 Nov 2012 ROI survey had the highest stack count (359) with the lowest uncertainty values
333 of ± 0.02 m/day (Table 2).

334 **4.1 July 2012 Surface Velocities**

335 The 6-7 July 2012 observations show slope-parallel velocities that range from ~ 0.0 -1.5 m/day for
336 both the Nisqually and Emmons glaciers (Fig. 3A, 4, 6). Both display high velocities over their
337 upper and central regions that taper into essentially stagnant (< 0.05 m/day) debris-covered
338 regions near the terminus. In general, slope-parallel velocities near the summit are small (< 0.2
339 m/day).

340 On the Nisqually Glacier, a series of local velocity maxima (> 1.0 m/day) are associated with
341 increased surface slopes between local surface highs. Local velocity maxima are also observed
342 for the fast-flowing Nisqually icefall (western branch of Upper Nisqually, see Fig. 3) and above
343 the Nisqually ice cliff (eastern branch). A relatively smooth velocity gradient from slow- to fast-
344 moving ice is present upstream of the icefall, while the velocities above the ice cliff display a
345 steep velocity gradient (Fig. 3).

346 The main (south) branch of the Emmons glacier displays generally increasing velocity from the
347 summit to lower elevations. A large high velocity region (> 0.7 -1.1 m/day) is present over central
348 Emmons, downstream of the confluence of upper branches. These elevated velocities decrease

349 at lower elevations, where ice thickness increases and surface slopes decrease (Fig. A5). A
350 central “core” of exposed ice displays slightly elevated velocities relative to surrounding debris-
351 covered ice within ~1-1.5 km of the terminus.

352 Velocities exceed 1 m/day over the “central” branch of the Upper Emmons Glacier, where flow
353 is restricted between two parallel bedrock ridges, with local maxima similar to Nisqually.

354 Velocities at higher elevations within the “central” branch appear slower (<0.1-0.5 m/day),
355 separated from the fast downstream velocities by a small area that was excluded due to phase
356 unwrapping errors. Photographs show that this area appears heavily fractured with many large
357 blocks indicative of rapid, discontinuous flow (Fig. A3).

358 Smaller, relatively thin glaciers, such as the Fryingpan, Upper Kautz, and Inter Glacier (labeled
359 on Fig. 1), also display nonzero surface velocities of <0.1-0.2 m/day, but with limited spatial
360 variability.

361 **4.2 Seasonal variability**

362 The repeat observations from the ROI viewpoint provide time series that capture seasonal
363 velocity variability for the Nisqually, Wilson and Upper Kautz Glaciers. We observe significant
364 velocity changes during the summer to winter transition and more subtle changes within the
365 winter period. These changes are shown in map view on Fig. 4 and in profile view with
366 corresponding slope and ice thickness on Fig. 6.

367 These data show a velocity decrease of 0.2-0.7 m/day (-25 to -50%) from July to November 2012
368 for most of the Nisqually Glacier. This includes central and lower Nisqually and the ice above
369 the ice cliff. The greatest velocity decreases are observed near the crest and lee of surface rises
370 (downstream of data gaps from radar shadows, Fig. 4), where some of the highest velocities were
371 observed in July. In contrast, the area immediately downstream of the ice cliff and the area
372 surrounding the icefall both display an apparent velocity increase for the same time period (Fig.
373 4, 6). While the increase is less than the 95% confidence interval for most areas, we can
374 confidently state that the icefall and area below the ice cliff do not display the significant
375 decrease in velocity observed elsewhere.

376 The majority of the Wilson Glacier displays a similar ~0.3-0.7 m/day (-40 to -60%) velocity
377 decrease from July to November. Interestingly, the steep transition where the Wilson merges

378 with the Nisqually displays an apparent velocity increase of ~ 0.1 m/day during this time period
379 (Fig. 4). These data also reveal subtle velocity increases in the debris-covered ice near the
380 Nisqually terminus and the Upper Kautz glacier (Fig. 4), though these increases are statistically
381 insignificant.

382 The repeat winter observations of Nisqually show relatively constant velocities with some
383 notable variability. Analysis of the 2 Nov. to 10 Dec. observations reveals a statistically
384 significant -0.1 m/day (-50%) velocity decrease ~ 1 km upstream of the terminus (centered on
385 ~ 0.7 km in Fig. 6A profile), a $+0.1$ to $+0.2$ m/day ($+20$ to $+30\%$) increase over central Nisqually
386 centered on ~ 3.5 km in the Fig. 6D profile, and an apparent $+0.2$ m/day ($+130\%$) increase over
387 the Upper Wilson. In the latter case, the 10 Dec. velocities are actually higher than those
388 observed in July. The slowdown over lower Nisqually appears robust, but other trends have
389 amplitudes that are mostly below the 95% confidence interval for the 27 Nov. and 10 Dec.
390 observational campaigns (Fig. 4).

391 **4.3 Diurnal variability**

392 We collected ~ 21 and ~ 24 hour time series for the Emmons and Nisqually/Wilson Glaciers
393 (Table 1) in July and November, respectively, and look at changes throughout the day. Although
394 uncertainties are large, we present the time series on Fig. 7.

395 In general, velocities for these regions remain relatively constant during their respective
396 sampling periods. The Emmons time series shows an apparent decrease in velocity over the
397 central, fast-flowing regions (B, C, D in Fig. 7A) from $\sim 18:00$ to $21:00$ local time, and an
398 apparent increase between $\sim 07:00$ to $09:00$ local time (Fig. 7A). The Nisqually time series
399 shows an apparent decrease from $\sim 06:00$ to $11:00$ local time for the icefall and ice cliff, and an
400 apparent decrease for several areas of the glaciers followed by an increase (Fig. 7B). However,
401 uncertainties are large and none of these are statistically significant.

402 **4.4 Comparison with independent velocity measurements**

403 We now compare our TRI results with independent velocity measurements for an overlapping
404 time period. Walkup et al. (2013) performed repeat total station surveys to document the
405 location of sparse supraglacial cobbles and boulders on the lower Nisqually glacier from 2011-
406 2012. While measurement errors (e.g., cobble rolling/sliding) for these observations are difficult

407 to document, the large sample size and relatively long measurement intervals allow for accurate
408 surface velocity estimates.

409 Figure 8 shows average velocity vectors measured by Walkup et al. (2013) for the period
410 between 19 July and 11 October 2012, with corresponding surface-parallel velocity vectors from
411 the 7 July and 2 November TRI surveys. This comparison is summarized on Table 4. In general,
412 the velocity magnitudes are similar, with the overall mean of the Walkup et al. (2013)
413 measurements slightly higher on average, but often falling between the 7 July and 2 November
414 GPRI magnitudes, as would be expected of a mean velocity spanning approximately the same
415 period. The velocity directions are also relatively consistent, with a median angular difference of
416 12° . The greatest deviations are observed near the ice margins and over small-scale local
417 topography (e.g. ice-cored moraine near western margin), where surface-parallel flow
418 assumptions break down. In general, the two techniques provide similar results and offer
419 complementary data validation. However, since the Walkup et al. (2013) measurements were
420 limited to accessible areas, they cannot be used to validate TRI observations for heavily
421 crevassed areas, icefalls, and other hazardous dynamic areas generally higher on the mountain.

422 **4.5 2-D flow modeling**

423 Figure 9 shows modeled deformation, sliding velocity residual (observations - deformation
424 model), and sliding percent (sliding velocity residual as percentage of total velocity) with best
425 estimate model parameters for Nisqually glacier in July and November. Figure 10 shows
426 corresponding output for Emmons. The SIA deformation models suggest that most areas of both
427 glaciers are moving almost entirely by sliding. The modeled glacier deformation alone is unable
428 to account for the observed surface velocity during any of the observation periods. Only a
429 median of 1% of the velocity field over the Nisqually glacier area can be explained by internal
430 deformation in July, and only 2% in November. If we consider $\pm 25\%$ ice thickness and up to 2x
431 the ice softness, the possible range of the median deformation contribution is still small, 0.5 –
432 7% in July and 0.5 – 8 % in November. If we consider only $\pm 25\%$ ice thickness and do not
433 change the ice softness, the range narrows to 0.5 – 4% in both cases. Using stake measurements,
434 Hodge (1974) estimated deformation contributed $\sim 5\text{-}20\%$ of the velocity for the upper third of
435 the ablation area of the Nisqually glacier. He did not study any areas above the equilibrium line,
436 so to compare directly to Hodge's (1974) numbers, we take the median deformation percentage

437 over approximately the upper third of the ablation area and find a best estimate of 1% (range 0.3
438 – 5%) for July and 2% (range 0.5 – 7%) for November. These numbers suggest that sliding is
439 even more dominant than Hodge (1974) estimated in this area, though it is difficult to say if the
440 differences are real (i.e. sliding was higher in 2012 than it was five decades ago) or just due to
441 differences in methods and assumptions.

442 The model results for Emmons suggest that deformation is more important for the Emmons
443 glacier than for Nisqually. A median of 9% of the July velocity field of Emmons can be
444 explained by deformation, with a possible range of 3 – 40% when considering $\pm 25\%$ ice
445 thickness and up to 2x the ice softness. If we consider only $\pm 25\%$ ice thickness, the range
446 narrows to 3 – 20%.

447 There are a few regions where the observed surface velocity can be explained entirely or nearly
448 entirely by internal deformation. These include the area within ~1-2 km of the Nisqually and
449 Emmons Glacier terminus, where ice is relatively thick and observed velocities are small.

450 **5. Discussion**

451 The continuous coverage of the TRI provides information about the spatial distribution of
452 surface velocities and strain rates. Several local velocity maxima are apparent along the
453 centerline of the Nisqually glacier and the central branch of the Emmons glacier. These velocity
454 maxima are associated with surface crevasses and increased surface slopes, with peak velocities
455 typically observed just upstream of peak slope values (Fig. 6). They are likely related to
456 accelerated flow downstream from local bedrock highs,

457 However, the local velocity maxima at ~2.1 km in Fig. 6 corresponds to a region of decreased
458 surface slopes and increased ice thickness. This location also displayed significant seasonal
459 velocity change, which could be related to variations in local subglacial hydrology (e.g. reservoir
460 drainage) during this time period.

461 **5.1 Icefall and ice cliff dynamics**

462 Terrestrial radar interferometry offers new observations over dynamic, inaccessible areas that
463 have received limited attention in previous studies (e.g., icefalls, ice cliffs). For example, the
464 velocities above the Nisqually ice cliff display an abrupt transition from slow- to fast-moving ice
465 (Fig. 4). The high strain rates associated with this transition are suggestive of crevasse opening

466 and “detached slab” behavior rather than continuous flow, which is reflected in the heavily
467 crevassed surface at this location.

468 Our results show that the Nisqually icefall and the icefall at the convergence of the Wilson and
469 Nisqually glaciers show a slight increase in velocity from July to the winter months. This
470 suggests that the icefalls may not be susceptible to the same processes that caused the seasonal
471 velocity decrease over much of the rest of the glacier. This may indicate that there is a lack of
472 local continuity through icefalls, which appears to prevent or dampen propagation of
473 downstream seasonal velocity decreases. It could also indicate that the icefall is relatively well-
474 drained year-round, and is not significantly affected by seasonal changes in subglacial
475 hydrology. A potential explanation for the observed minor increase in velocity could be early
476 winter snow accumulation on blocks within the icefall.

477 Interestingly, in contrast to the icefall, the hanging glacier above the Nisqually ice cliff displayed
478 a significant velocity decrease from July to November, despite similar steep surface slopes and
479 crevasse density. This could potentially be related to the lack of backstress from downstream ice
480 and an increased sensitivity to minor fluctuations in subglacial hydrology. Hanging glaciers are
481 also thought to be the source of some of the repeating glacial earthquakes that are triggered by
482 snow loading (Allstadt and Malone, 2014), which highlights their sensitivity to minor
483 perturbations.

484 **5.2 Lack of significant diurnal variability**

485 We expected to see significant variability over the 24-hour July time series for Emmons, as
486 atmospheric temperatures varied from 16°C to 27°C at Paradise Visitors Center (~1600 m.a.s.l),
487 and skies remained cloud-free during data collection. We hypothesized that the resulting
488 increase in meltwater input from late morning through late afternoon might produce an
489 observable increase in sliding velocity. While the results potentially show a slight velocity
490 decrease at higher elevations overnight, and a slight velocity increase in the morning (Fig. 7A,
491 A-D), these changes are not statistically significant, nor coincident with times expected to have
492 highest melt input. The lack of a significant diurnal speedup suggests that the subglacial conduits
493 are relatively mature by July, and are capable of accommodating the diurnal variations in
494 meltwater flux without affecting basal sliding rates.

495 We did not expect to see significant diurnal changes in the 21-hour November time series for
496 Nisqually (Fig. 7A), as atmospheric temperatures ranged between 2°C and 6°C at Paradise
497 Visitors Center (~1600 m a.s.l.) and skies were partly-cloudy to overcast during data collection,
498 so surface meltwater input should have been minimal. Our results show only a minor velocity
499 decrease higher on the glacier in the morning hours but it is not statistically significant and does
500 not occur at times when we would expect increased meltwater.

501 Though some of the subtle changes in the extended time series may reflect actual diurnal
502 velocity variability, we cannot interpret these with confidence. This suggests that the magnitude
503 of diurnal variability, if it exists, during these time periods is minor when compared to the
504 observed seasonal changes. It also implies that other stacks derived from a subset of the day can
505 be considered representative of the daily mean, and can be compared for seasonal analysis.

506 **5.3 Seasonal velocity changes**

507 The observed seasonal velocity changes from July to November can likely be attributed to
508 changes in glacier sliding, which in turn are driven by evolving englacial and subglacial
509 hydrology (Fountain and Walder, 1998). During the spring-summer months, runoff from
510 precipitation (i.e. rain) and surface snow/ice melt enters surface crevasses, moulins, and/or
511 conduits near the glacier margins. This water travels through a series of englacial fractures,
512 reservoirs and conduits, and eventually ends up in a subglacial network of channels and
513 reservoirs between the ice and bed. Storage time and discharge rates within the subglacial
514 system are variable, with water finally exiting the system through one or more proglacial streams
515 at the terminus. This dynamic system is continuously evolving due to variable input, storage
516 capacity, and output. In early July, ongoing snowmelt should produce high meltwater discharge
517 that travels through a relatively efficient network of mature conduits. As discharge decreases
518 later in the summer, these subglacial conduits/reservoirs close due to ice creep without high flow
519 to keep them open through melting due to heat from viscous dissipation. By November, there
520 should be little or no surface meltwater input and we would expect to see a minimum in basal
521 sliding velocity (Hodge, 1974). This is consistent with the observed velocity decrease in Fig. 4.
522 However, the deformation modeling results (Fig. 9) show that a significant sliding component is
523 still present for most of the Nisqually glacier in November and December, when minimum
524 surface velocities are expected.

525 The spatial patterns of the velocity change observed between July and November can be used to
526 infer the extent of basal sliding. This may provide some insight into subglacial water storage,
527 since the deformation component of surface velocity should remain nearly the same year-round.
528 Fig. 4 indicates that almost the entire Nisqually glacier slows down significantly between July
529 and November, suggesting that storage is occurring under most of the glacier below the icefall
530 and ice cliff. Significant velocity decreases are observed near local surface rises (Fig. 4), where
531 some of the highest velocities were observed in July. This suggests that there are likely
532 subglacial cavities downstream of these areas with high basal water pressures that can support
533 enhanced sliding during the summer.

534 Hodge (1974) interpreted a delay in both the maximum summer velocity and minimum winter
535 velocity between the terminus and ELA as a propagating “seasonal wave” traveling ~55 m/day.
536 While our sampling is limited, the continued November 2 to November 27 slowdown over the
537 lower Nisqually near the terminus (Fig. 4F) could represent a delayed response to the significant
538 slowdown over central Nisqually. This might be expected, as surface velocities near the terminus
539 are dominated by internal deformation and should respond more slowly than areas dominated by
540 basal sliding.

541 **5.4 Comparison with historical velocity measurements**

542 As described earlier, Hodge (1972, 1974) measured surface velocity for a network of centerline
543 stakes on the lower Nisqually from 1968-1970. He documented a significant seasonal cycle with
544 minimum velocities in November and maximum velocities in June.

545 To put our velocity data in historical context, we digitized Hodge’s (1972) July and November
546 1969 surface velocity data at 19 stake locations along a profile of the lower half of the Nisqually
547 glacier. We then sampled the 2012 TRI slope-parallel velocities at these locations (Fig. 11).

548 Remarkably, in spite of significant terminus retreat of up to ~360 m and surface elevation
549 changes of approximately -20 m (Sisson et al., 2011), the November 1969 and November 2012
550 surface velocities are almost identical at stakes 12-20, suggesting that bed properties and local
551 geometry have greater influence over sliding velocity than ice thickness or relative distance from
552 the terminus. In contrast, the July 2012 velocities at stakes 12-20 are 8-33% faster than the July
553 1969 velocities. The ice is mostly sliding at these locations, so the change could be related to a
554 difference in the timing of the peak summer velocities, or potentially enhanced sliding in 2012.

555 The nearly identical surface velocities in November 1969 and 2012 suggests that the discrepancy
556 between Hodge's sliding percentage estimates and our estimates (section 4.5) is likely related to
557 different methodology and assumptions rather than actual changes in sliding since 1969.

558 The most notable difference between the profiles is observed closer to the terminus at stakes 7-
559 12. At these locations, the July and November 2012 velocities are both <0.05 m/day, whereas
560 July and November 1969 velocities are ~ 0.2 and ~ 0.1 m/day, respectively, with significant
561 seasonal variability. This suggests that the ice near the present-day terminus is essentially
562 stagnant and no longer strongly influenced by changes in subglacial hydrology.

563 **6. Conclusions**

564 In this study, we used repeat TRI measurements to document spatially continuous velocities for
565 the Emmons and Nisqually glaciers at Mount Rainier, WA. We produced surface velocity maps
566 that reveal speeds of >1.0 - 1.5 m/day over the upper and central regions of these glaciers, <0.2
567 m/day near the summit, and <0.05 m/day over the stagnant ice near their termini. Novel data
568 processing techniques reduced uncertainties to ± 0.02 - 0.08 m/day, and the corrected, surface-
569 parallel TRI velocities for Nisqually display similar magnitude and direction with a set of sparse
570 interannual velocity measurements (Walkup et al., 2013).

571 Repeat surveys show that Nisqually glacier surface velocities display significant seasonal
572 variability. Most of the glacier experienced a ~ 25 - 50% velocity decrease (up to -0.7 m/day)
573 between July and November. These seasonal variations are most likely related to changes in
574 basal sliding and subglacial water storage. Interestingly, the steep icefall displays no velocity
575 change or even a slight velocity increase over the same time period. We documented no
576 statistically significant diurnal velocity variations in ~ 24 -hour datasets for Nisqually and
577 Emmons, suggesting that subglacial networks efficiently handled diurnal meltwater input.

578 Comparisons with 1969 velocity measurements over the Lower Nisqually (Hodge, 1972; 1974)
579 reveal similar November velocities in both 2012 and 1969, and faster July velocities in 2012.

580 Using a simple 2D ice flow model, we estimate that basal sliding is responsible for most of the
581 observed surface velocity signal except in a few areas, mainly near the termini. The model
582 suggests that about 99% of the July velocity field for the Nisqually glacier is due to sliding. Even
583 when we account for the large uncertainties in ice thickness and ice softness, the possible range

584 of sliding percentage is still narrow: 93 – 99.5% Deformation is more important for the Emmons
585 glacier, where we estimate 91% of the observed motion is due to sliding, with a much wider
586 possible range of 60 – 97% when accounting for uncertainties.

587 In summary, TRI presents a powerful new tool for the study of alpine glacier dynamics. With
588 just a few hours of fieldwork for each survey, we were able to document the dynamics of several
589 glaciers at Mount Rainier in unprecedented extent and detail from up to 10 km away. TRI is
590 particularly well suited for examining diurnal and seasonal glacier dynamics, especially for areas
591 that are difficult to access directly (e.g., icefalls), like many parts of the glaciers at Mount
592 Rainier. Repeat surveys provide precise surface displacement measurements with unprecedented
593 spatial and temporal resolution, offering new insight into complex processes involving subglacial
594 hydrology and basal sliding. Future studies involving coordinated, multi-day TRI occupations
595 during critical seasonal transition periods could undoubtedly provide new insight into these and
596 other important aspects of alpine glaciology.

597 **Figure Captions**

598 Figure 1. Glaciers at Mount Rainier and locations of viewpoints used for ground based radar
599 interferometry. Instrument view angle ranges are indicated by arrows extending away from each
600 viewpoint location. Boxes A-C show zoom areas for later figures. Inset map shows regional
601 location of Mount Rainier. Glacier outlines in this and subsequent figures are from Robinson et
602 al. (2010).

603 Figure 2. GPRI equipment setup during 27 Nov 2012 campaign at ROI viewpoint.

604 Figure 3. A) Median slope-parallel velocity derived from TRI for GLPEEK and SUNRIZ
605 viewpoints taken on July 6-7, 2011. B) Width of 95% confidence interval (high minus low limits
606 for slope parallel flow field) of slope parallel velocities for July 6-7, 2011 computed by
607 bootstrapping after performing atmospheric noise corrections and stacking. Area shown is
608 indicated by Box A on Fig. 1.

609 Figure 4. A-D) Median slope-parallel velocities for Nisqually and Wilson glaciers for four
610 different time periods taken from ROI viewpoint. Dashed lines on top left panel show locations
611 of profiles taken to create Fig. 6, markers indicate distance in km. E-G) Percent change in
612 median slope-parallel velocity for the Nisqually and Wilson glaciers between time periods. Blue

613 indicates a velocity decrease and red indicates a velocity increase relative to the earlier time
614 period, gray polygons indicate areas where velocity change is significant with 95% confidence.
615 Area shown is indicated by Box B on Fig. 1.

616 Figure 5. Width of 95% confidence interval (high minus low limits for slope parallel velocity)
617 over Nisqually glacier computed by bootstrapping. Shown for four sampling periods from the
618 ROI viewpoint. Note that the color bar is scaled differently than Fig. 3B.

619 Figure 6. A and C: Slope parallel velocity profiles along the two branches of Nisqually glacier
620 (profile lines shown in map view on Fig. 4A) for all sample time periods and viewpoints. B and
621 D: Surface slope and ice thickness along each profile line. Surface slope is smoothed identically
622 to that used for slope parallel corrections (see text), ice thicknesses are estimated from digitized
623 basal contours from Driedger and Kennard (1986) and surface elevations from the 2007/2008
624 LiDAR (Robinson et al., 2010). Refer to Figure 5 and Table 2 for uncertainty estimates.

625 Figure 7. LOS velocity time series for areas outlined on maps to the right. Shaded region around
626 each line represents \pm one standard error for a 2-hour running mean. a) 24-hour timeseries at
627 SUNRIZ on July 7-8, 2012, gray box indicates the period with poor data quality (see text for
628 details). b) 22-hour timeseries at ROI on Nov 1-2, 2012.

629 Figure 8. Comparison of average azimuth and velocities measured by Walkup et al. (2013)
630 between 19 July 2012 and 11 October 2012 (black) compared to TRI slope-parallel velocities
631 derived from this study at the same locations for two time periods that bracket the time period
632 measured by Walkup et al. (2013). See Table 4 for comparison statistics and Box C on Fig. 1 for
633 context.

634 Figure 9. Model results for summer (6 July 2012) and a late fall (2 Nov 2012) time period for
635 Nisqually and Wilson glaciers. A, D) Modeled surface velocity for internal deformation, B, E)
636 Sliding residual (observed slope parallel velocity minus the modeled deformation velocity), C, F)
637 Estimate of the sliding percentage (sliding residual divided by total slope-parallel velocity).

638 Figure 10. Same as Fig. 9 but for Emmons Glacier.

639 Figure 11. July and November 1969 surface velocities measured by Hodge (1974, digitized from
640 Hodge, 1972) at 19 stake locations along lower Nisqually profile (circles), compared with
641 sampled 2012 slope-parallel velocities for corresponding locations/seasons (triangles). Stake

642 locations are labeled and indicated with dotted lines and are shown in map view at right (same
643 map extent as Fig. 8).

644 Figure A1. Photomosaic acquired from ROI viewpoint on July 5, 2012. Approximate glacier
645 outlines shown in red.

646 Figure A2. Photomosaic acquired from GLPEEK viewpoint on July 6, 2012. Approximate
647 glacier outlines shown in red.

648 Figure A3. Photomosaic acquired from SUNRIZ viewpoint on July 7, 2012. Approximate glacier
649 outlines shown in red.

650 Figure A4. Pair of multi-look intensity (MLI) radar images from ROI viewpoint (left and center)
651 generated from original single-look complex (SLC) images multi-looked by 15 samples in range
652 and multi-looked interferogram generated from the SLC images (right).

653 Figure A5. A) Filtered ice thickness and B) filtered slope used as model inputs.

654 **Appendix A**

655 Appendix A contains supplementary figures.

656 **Author Contribution**

657 K. E. Allstadt coordinated the effort, developed methods, performed data acquisition and
658 processing, made the figures and prepared the manuscript. D.E. Shean developed methods,
659 performed data acquisition, processing, analysis, and interpretation of results, and contributed
660 significantly to the manuscript. A. Campbell performed modeling experiments and contributed
661 the related section of the manuscript. M. Fahnestock and S. Malone contributed significantly to
662 experiment design, establishment of objectives, data acquisition, and manuscript review.

663 **Acknowledgements**

664 Many thanks to the National Park Service staff at Mount Rainier National Park, in particular
665 Scott Beason, Laura Walkup, and Barbara Samora. Justin Sweet and Zach Ploskey provided field
666 assistance. Ryan Cassotto and David Schmidt provided data processing guidance. The
667 University of Washington Glaciology group provided useful discussions. Thanks to M. Luthi and
668 A. Vieli for their thoughtful reviews and suggestions, which have significantly improved the
669 manuscript. Original data used in this analysis are available upon request from the corresponding

670 author. This work was supported in part by the U.S. Geological Survey under contract
671 G10AC00087 to the Pacific Northwest Seismic Network, the University of Washington Earth
672 and Space Sciences Department Awards, the Colorado Scientific Society, the Gordon and Betty
673 Moore Foundation (Grants 2626 and 2627), and the National Science Foundation under Award
674 No. 1349572 during the final part of manuscript preparation.

675 **References**

- 676 Allstadt, K. and Malone, S. D.: Swarms of repeating stick-slip icequakes triggered by snow
677 loading at Mount Rainier volcano, *J Geophys Res-Earth*, 119, 1180-1203,
678 doi:10.1002/2014JF00308, 2014.
- 679 Anderson, R. S., Anderson, S. P., MacGregor, K. R., Waddington, E. D., O'Neel, S., Riihimaki,
680 C. A., and Loso, M. G.: Strong feedbacks between hydrology and sliding of a small alpine
681 glacier, *J Geophys Res-Earth*, 109(F3), F03005, doi:10.1029/2004JF000120, 2014.
- 682 Bartholomaeus, T. C., Anderson, R. S., and Anderson, S. P.: Response of glacier basal motion to
683 transient water storage, *Nat Geosci*, 1, 33-37, doi:10.1038/ngeo.2007.52, 2008.
- 684 Burgmann, R.; Rosen, P.A.; Fielding, E.J.: Synthetic aperture radar interferometry to measure
685 Earth's surface topography and its deformation, *Annu Rev Earth PL SC*, 28, 169–209,
686 doi:10.1146/annurev.earth.28.1.169, 2000.
- 687 Caduff, R., Schlunegger, F., Kos, A., and Wiesmann, A.: A review of terrestrial radar
688 interferometry for measuring surface change in the geosciences, *Earth Surf Proc Land*,
689 doi:10.1002/esp.3656, 2014.
- 690 Crandell, D. R. and Fahnestock, R. K.: Rockfalls and Avalanches from Little Tahoma Peak on
691 Mount Rainier Washington, *Contribution to General Geology 1965*, Geological Survey Bulletin
692 1221-A, A1-A30, U.S Geological Survey, 1965.
- 693 Cuffey, K. M. and Paterson, W. S. B.: *The physics of glaciers*, 4th edition, Academic Press,
694 2010.
- 695 Driedger, C. L. and Kennard, P. M.: *Ice Volumes on Cascade Volcanoes: Mount Rainer, Mount*
696 *Hood, Three Sisters, Mount Shasta*, USGS Professional Paper 1365, 1986.
- 697 Efron, B.: Bootstrap Methods: Another Look at the Jackknife, *Ann Stat*, 7, 1-26,

698 doi:10.1214/aos/1176344552, 1979.

699 Fountain, A. G. and Walder, J. S.: Water flow through temperate glaciers, *Rev Geophys*, 36(3),
700 299-328, 1998.

701 Gagliardini, O., Zwinger, T., Gillet-Chaulet, F., Durand, G., Favier, L., de Fleurian, B., Greve,
702 R., Malinen, M., Martín, C., Råback, P., Ruokolainen, J., Sacchettini, M., Schäfer, M., Seddik,
703 H. and Thies, J.: Capabilities and performance of Elmer/Ice, a new-generation ice sheet model,
704 *Geosci. Model Dev.*, 6(4), 1299–1318, doi:10.5194/gmd-6-1299-2013, 2013.

705 Goldstein, R.: Atmospheric limitations to repeat-track radar interferometry, *Geophys Res Lett*,
706 22(18), 2517-2520, 1995.

707 Greve, R. and Blatter, H.: *Dynamics of Ice Sheets and Glaciers*, Springer, Berlin, Germany, doi:
708 10.1007/978-3-642-03415-2, 2009.

709 Heliker, C., Johnson, A., and Hodge, S.: *Nisqually Glacier, Mount Rainier, Washington, 1857-*
710 *1979: A Summary of the Long-Term Observations and a Comprehensive Bibliography*, USGS
711 *Open-file Report 83-541*, 20 p., U.S. Geological Survey, 1984.

712 Hodge, S.: *The movement and basal sliding of the Nisqually Glacier, Mt. Rainier: Seattle,*
713 *Wash., University of Washington, Department of Atmospheric Sciences Ph. D. dissertation,*
714 *1972.*

715 Hodge, S. M.: Variations in the sliding of a temperate glacier, *J Glaciol*, 13, 349-369, 1974.

716 Joughin, I. R., Kwok, R., and Fahnestock, M. A.: Interferometric estimation of three-dimensional
717 ice-flow using ascending and descending passes, *IEEE Transactions on Geoscience and Remote*
718 *Sensing*, 36(1), 25-37, doi:10.1109/36.655315, 1998.

719 Joughin, I.R., Smith, B.E., and Abdalati, W.: Glaciological advances made with interferometric
720 synthetic aperture radar, *J. Glaciol.*, 56(200), 1026-1042, 2010.

721 Kamb, B. and Echelmeyer, K., Stress-gradient coupling in glacier flow. I: longitudinal averaging
722 of the influence of ice thickness and surface slope, *J Glaciol*, 32(111), 267-284, 1986.

723 Le Meur, E., Gagliardini, O., Zwinger, T. and Ruokolainen, J.: Glacier flow modelling: a
724 comparison of the Shallow Ice Approximation and the full-Stokes solution, *Comptes Rendus*
725 *Phys.*, 5(7), 709–722, doi:10.1016/j.crhy.2004.10.001, 2004.

726 Massonnet, D. and Feigl, K.L.: Radar interferometry and its application to changes in the Earth's
727 surface, *Rev Geophys* 36(4), 441-500, doi: 10.1029/97RG03139, 1998.

728 Meier, M. F., and Tangborn, W. V.: Distinctive characteristics of glacier runoff, U.S. Geological
729 Survey Professional Paper 424-B, 14-16, 1961.

730 National Park Service: Annual Snowfall Totals at Paradise, 1920 to 2013, Dept. of the Interior
731 [<http://www.nps.gov/mora/planyourvisit/upload/Annual-snowfall-totals-July13.pdf>], last
732 accessed 29 Nov 2014, 2013.

733 Noferini, L., Mecatti, D., Macaluso, G., Pieraccini, M., and Atzeni, C.: Monitoring of Belvedere
734 Glacier using a wide angle GB-SAR interferometer, *J Appl Geophys*, 68(2), 289-293,
735 doi:10.1016/j.jappgeo.2009.02.004, 2009.

736 Nylén, T.H.: Spatial and Temporal Variations of Glaciers (1913-1994) on Mt. Rainier and the
737 Relation with Climate, Portland State University, Department of Geology, Masters thesis. 2004

738 Riedel, J., Long Term Monitoring of Glaciers at Mount Rainier National Park, Narrative and
739 Standard Operating Procedure Version 1.0, Natural Resource Report NPS/NCCN/NRR-
740 2010/175, National Park Service, Fort Collins, Colorado, 2010.

741 Riedel, J. and Larrabee, M. A.: Mount Rainier National Park Annual Glacier Mass Balance
742 Monitoring, Water Year 2011, North Coast and Cascades Network, Natural Resource Technical
743 Report NPS/NCCN/NRDS—2015/752, National Park Service, Fort Collins, Colorado, 2015.

744 Riesen, P., Strozzi, T., Bauder, A., Wiesmann, A., and Funk, M.: Short-term surface ice motion
745 variations measured with a ground-based portable real aperture radar interferometer, *J Glaciol*,
746 57(201), 53-60, doi:10.3189/002214311795306718, 2011.

747 Robinson, J. E., Sisson, T. W., and Swinney, D. D.: Digital topographic map showing the extents
748 of glacial ice and perennial snowfields at Mount Rainier, Washington, based on the LiDAR
749 survey of September 2007 to October 2008, US Geological Survey Digital Data Series 549,
750 United States Geological Survey, 2010.

751 Shean, D. E., Z. Moratto, O. Alexandrov, I. R. Joughin, B. E. Smith, P. J. Morin, and C. C.
752 Porter (in prep), An automated, open-source pipeline for mass production of digital elevation
753 models from very-high-resolution commercial stereo satellite imagery, *ISPRS J. Photogramm.*
754 *Remote Sens.*

755 Sisson, T., Robinson, J., and Swinney, D.: Whole-edifice ice volume change AD 1970 to
756 2007/2008 at Mount Rainier, Washington, based on LiDAR surveying, *Geology*, 39(7), 639-642,
757 doi:10.1130/G31902.1, 2011.

758 Swanson, D. A., Malone, S. D., and Samora, B. A.: Mount Rainier: a decade volcano, *Eos*,
759 *Transactions American Geophysical Union*, 73(16), 177-186, 1992.

760 Veatch, F.: Analysis of a 24-Year Photographic Record of Nisqually Glacier, Mount Rainier
761 National Park, Washington, Geological Survey Professional Paper 631, United States Geological
762 Survey, 1969.

763 Voytenko, D., Dixon, T.H., Howat, I.M., Gourmelen, N., Lembke, C., Werner, C.L., De la Pena,
764 S., Oddsson, B.: Multi-year observations of Breidamerkurjokull, a marine-terminating glacier in
765 southeastern Iceland, using terrestrial radar interferometry, *J. Glaciol*, 61(225), 42-54,
766 doi:10.3189/2015JoG14J099, 2015.

767 Walkup, L. C., Beason, S. R., Kennard, P. M., Ohlschlager, J. G., and Stifter, A. C.: Surficial Ice
768 Velocities of the Lower Nisqually Glacier and their Relationship to Outburst Flood Hazards at
769 Mount Rainier National Park, Washington, United States, Paper 240-3, 2013 GSA Annual
770 Meeting Abstracts, Denver, 2013.

771 Werner, C., Strozzi, T., Wiesmann, A., and Wegmuller, U.: A real-aperture radar for ground-
772 based differential interferometry, *Radar Conference, 2009 IEEE*, Pasadena, 3, 1-4, doi:
773 10.1109/RADAR.2009.4977136, 2008.

774 Werner, C., Wiesmann, A., Strozzi, T., Kos, A., Caduff, R., and Wegmiuler, U: The GPRI multi-
775 mode differential interferometric radar for ground-based observations, *Synthetic Aperture Radar*,
776 2012, EUSAR. 9th European Conference on, 304-307, 2012.

777 Zebker, H.A., Rosen, P.A., and Hensley, S.: Atmospheric effects in interferometric synthetic
778 aperture radar surface deformation and topographic maps, *J Geophys Res-Solid* 102.B4, 7547-
779 7563, doi: 10.1029/96JB03804, 1997.

780 Zwinger, T., Greve, R., Gagliardini, O., Shiraiwa, T. and Lyly, M.: A full Stokes-flow thermo-
781 mechanical model for firn and ice applied to the Gorshkov crater glacier, Kamchatka, *Ann.*
782 *Glaciol.*, 45(1), 29–37, 2007.

783

784 Table 1 Survey parameters

Sampling Location	Start Time (UTC)	End Time (UTC)	Survey length (hr)	Latitude	Longitude	Elev (m)	Glaciers in view	Sampling Interval (mins)	Number of Scans	Azimuth sweep	Chirp length (ms)	Chirp Band width (Hz)	Antennae angle
GLPEEK	7/6/12 17:20	7/6/12 23:37	6.3	46.7924	-121.7399	1788	Nisqually, Wilson	3	105	75°	4	50	+15°
SUNRIZ	7/7/12 19:50	7/8/12 19:56	24.1	46.9157	-121.6492	1929	Emmons, Winthrop	3	436	29°	8	25	+5°
ROI	7/6/12 0:32	7/6/12 5:23	4.8	46.7836	-121.7502	1564	Nisqually, Wilson	3	62	68°	4	50	+15°
ROI	11/2/12 1:20	11/2/12 23:14	21.9	46.7837	-121.7502	1559	Nisqually, Wilson	3	377	52°	4	50	+15°
ROI	11/27/12 18:47	11/28/12 0:29	5.7	46.7836	-121.7502	1563	Nisqually, Wilson	3	107	60°	4	50	+15°
ROI	12/10/12 20:50	12/11/12 1:32	4.7	46.7836	-121.7502	1562	Nisqually, Wilson	3	91	70°	4	50	+15°

785
786

787 Table 2 Summary of uncertainty estimates of median stacks

Sampling Location	Start Time (UTC)	End Time (UTC)	Total interferograms used/total collected	Median confidence interval width over ice* (m/day)	
				Before correction^	After correction
GLPEEK	7/6/12 17:20	7/6/12 23:37	93/105	0.23	0.07
SUNRIZ	7/7/12 19:50	7/8/12 19:56	215/436	0.14	0.09
ROI	7/6/12 0:32	7/6/12 5:23	56/62	0.33	0.11
ROI	11/2/12 1:20	11/2/12 23:14	359/377	0.16	0.04
ROI	11/27/12 18:47	11/28/12 0:29	100/107	0.44	0.10
ROI	12/10/12 20:50	12/11/12 1:32	76/91	0.43	0.15

* derived from bootstrapping, 95% confidence, line of sight velocities

^ correction refers to removing displacements due to atmospheric noise (interpolated over static control surfaces)

788

789 Table 3 Constants used in modeling analysis

Name	Symbol	Value	Units
Ice softness parameter	A	2.4×10^{-24}	$\text{Pa}^{-3} \text{s}^{-1}$
Side length of reference window	A_w	120	m
Acceleration of gravity	g	9.81	m s^{-2}
Coupling length	l	60	m
Flow law exponent	n	3	dimensionless
Density of ice	ρ_i	900	kg m^{-3}
Density of water	ρ_w	1000	kg m^{-3}

790

791 Table 4 Comparison between Walkup et al. (2013) and TRI velocities at Walkup et al. (2013)

792 sample locations (Figure 8)

Source	Velocity Magnitude (cm/day)				Angular Difference from Walkup et al. 2013 (degrees)			
	Mean	Median	Max	Min	Mean	Median	Max	Min
Walkup et al. 2013	22.3	16.6	64.4	1.8	-	-	-	-
GLPEEK July	20.8	10.5	82.9	0.1	15.8	12.0	55.8	0.7
ROI Nov	14.6	10.4	51.4	0.3	15.8	12.0	55.8	0.7

793

Figure 1

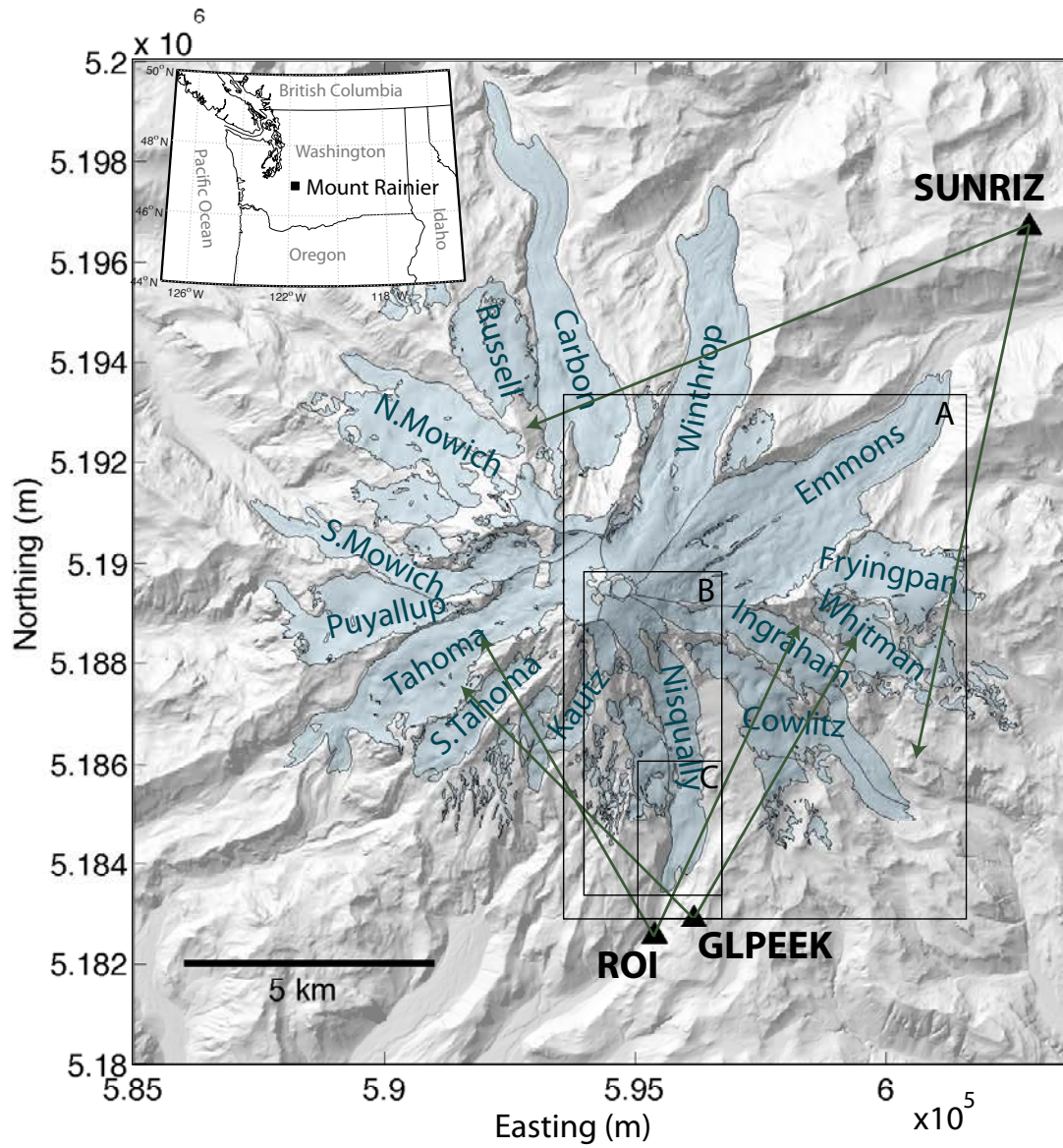


Figure 2

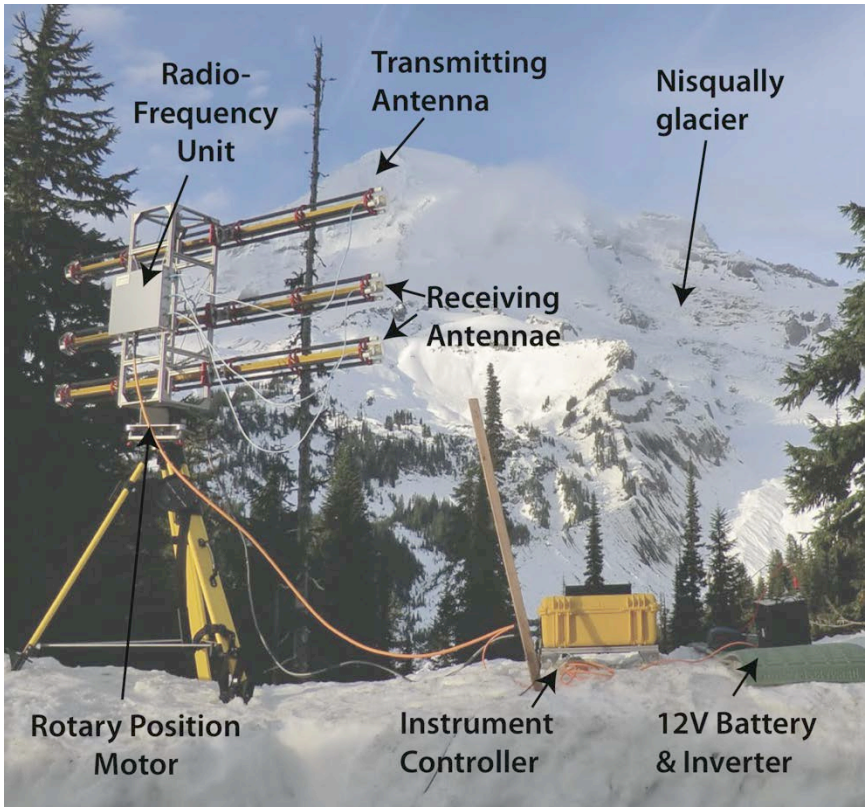


Figure 3

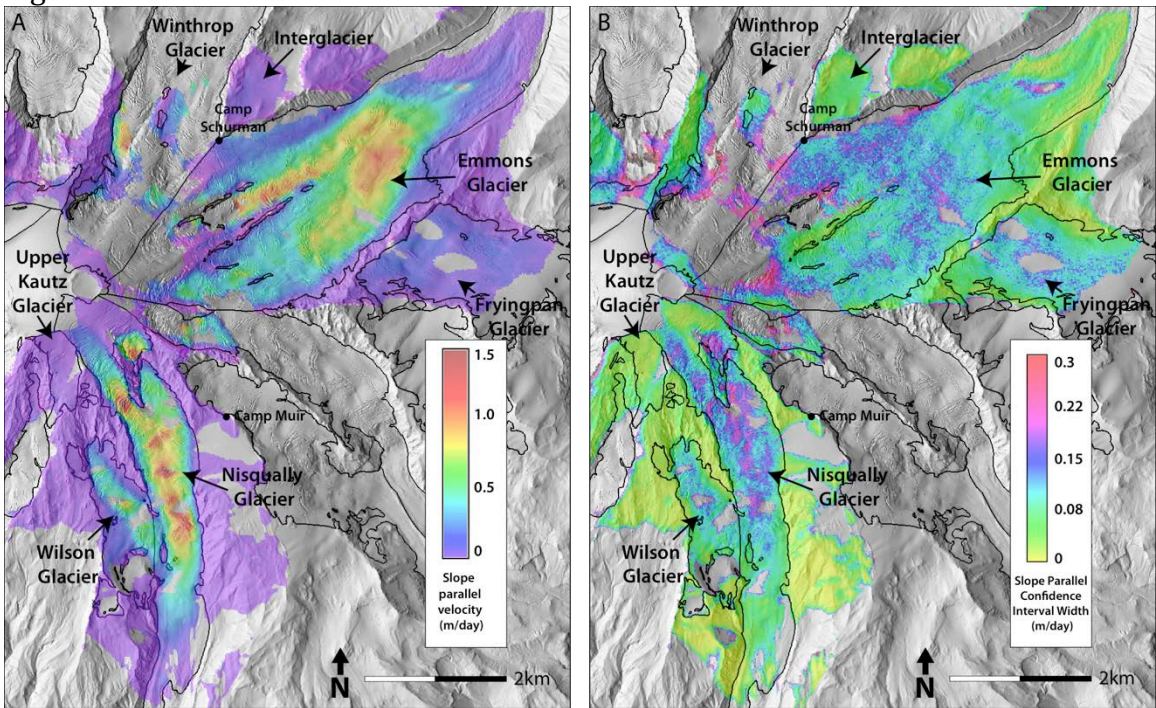


Figure 4

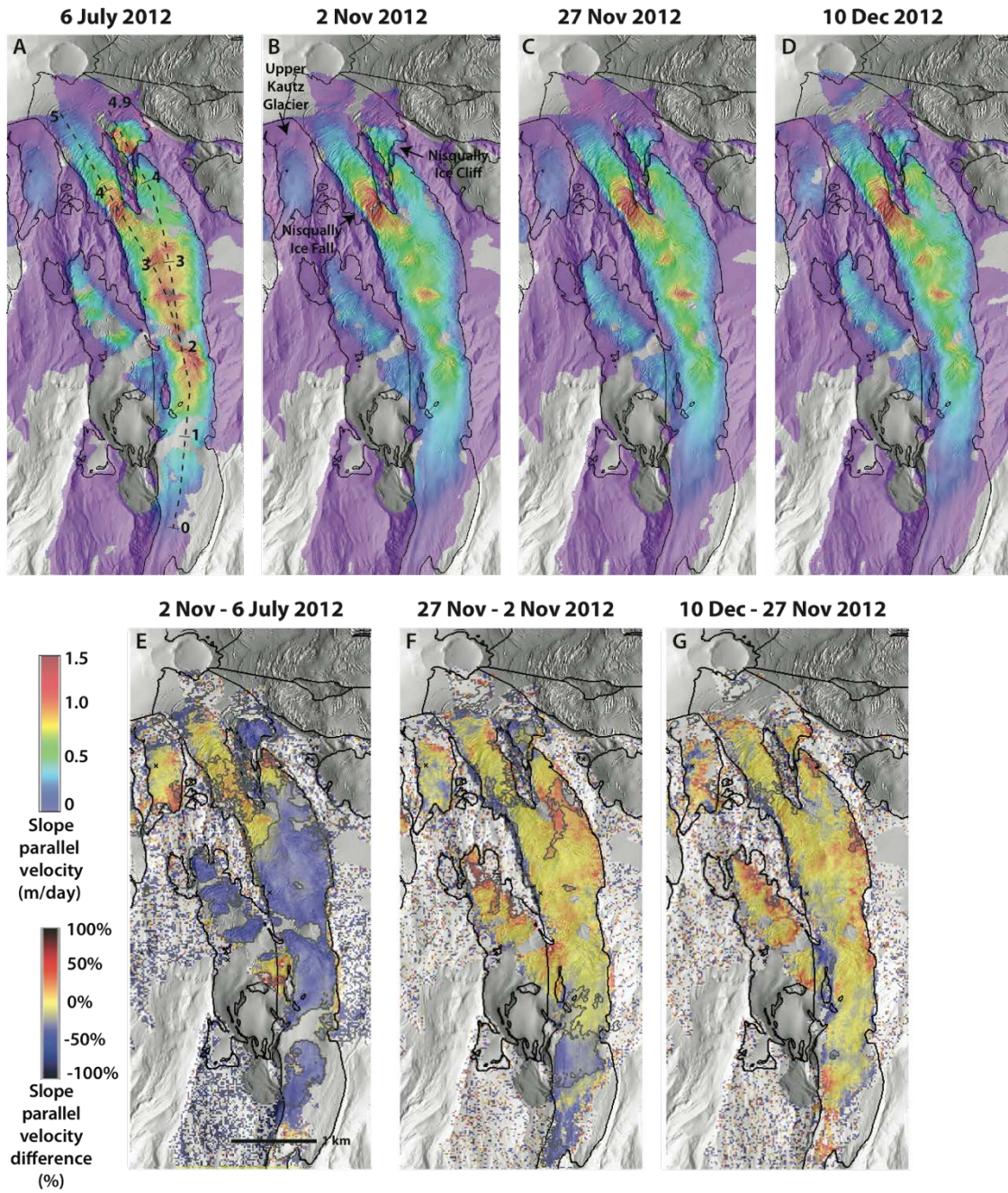


Figure 5

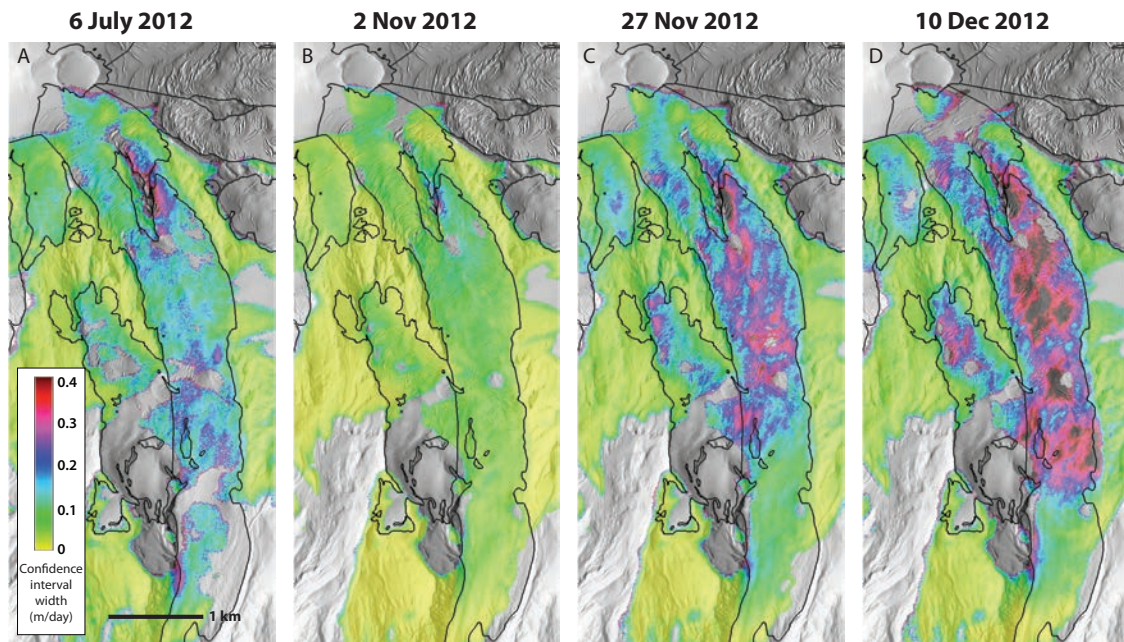


Figure 6

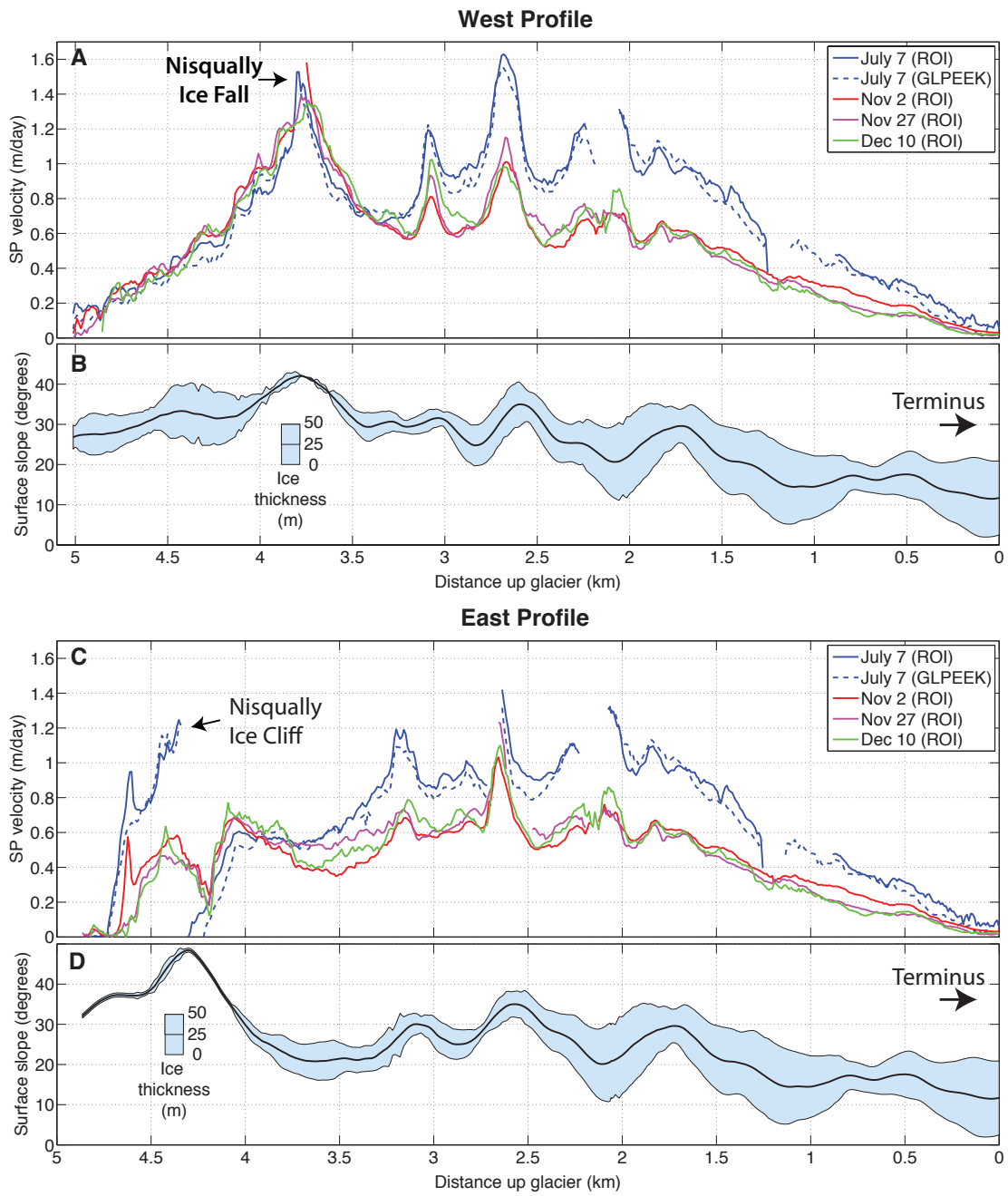


Figure 7

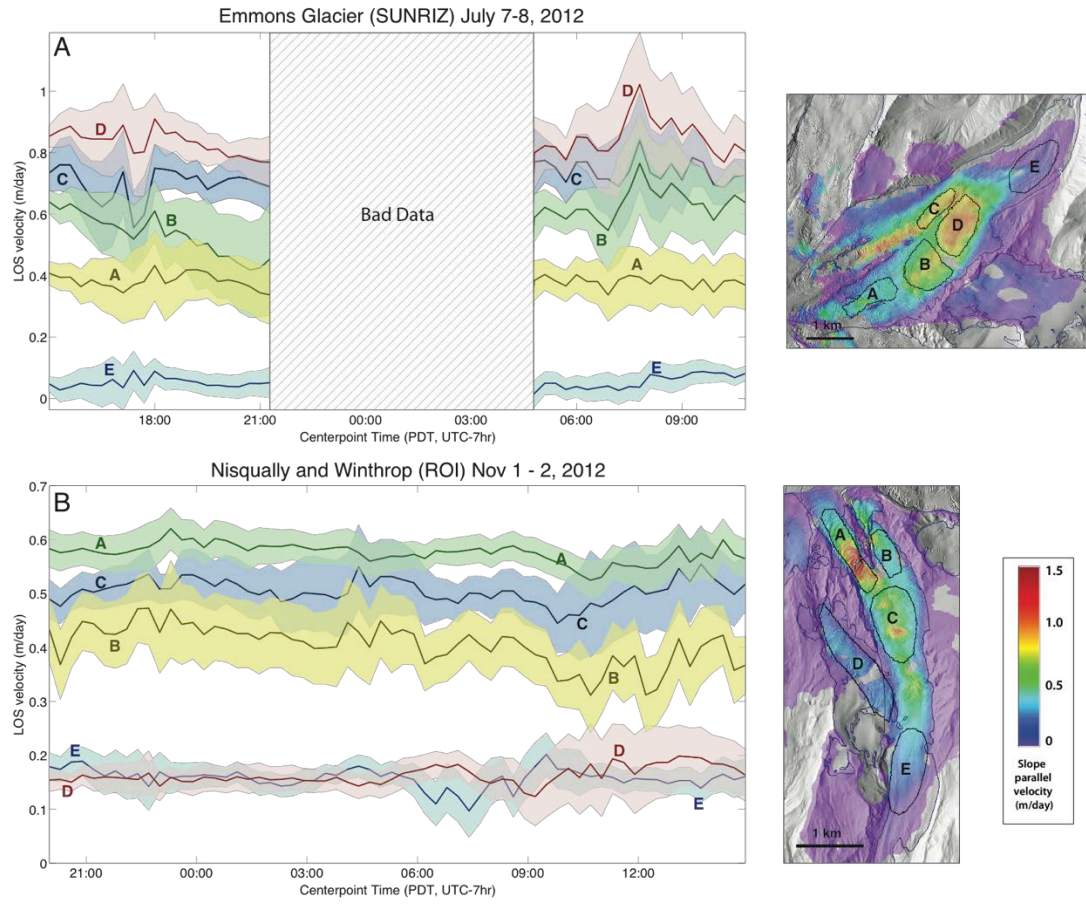


Figure 8

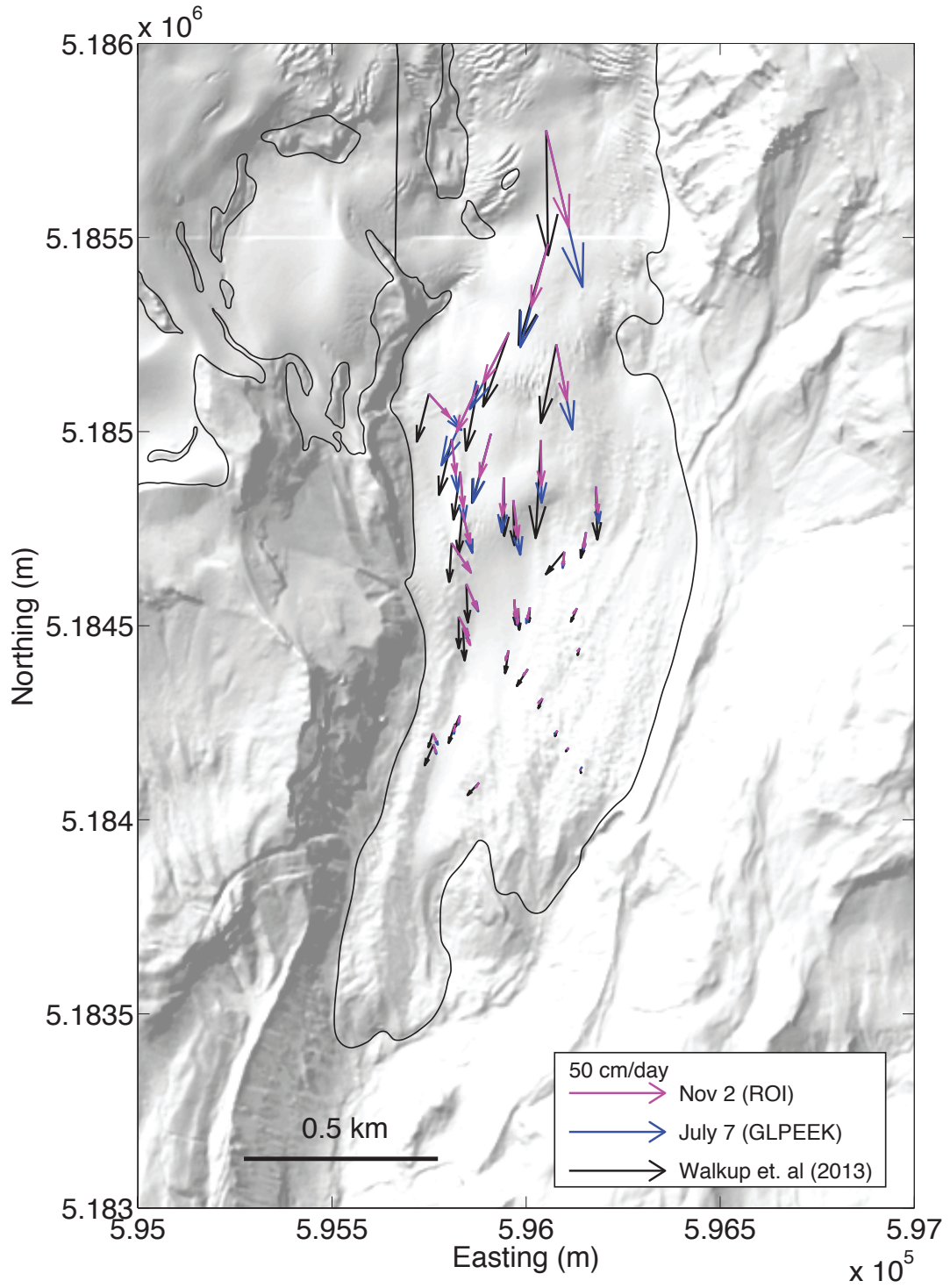


Figure 9

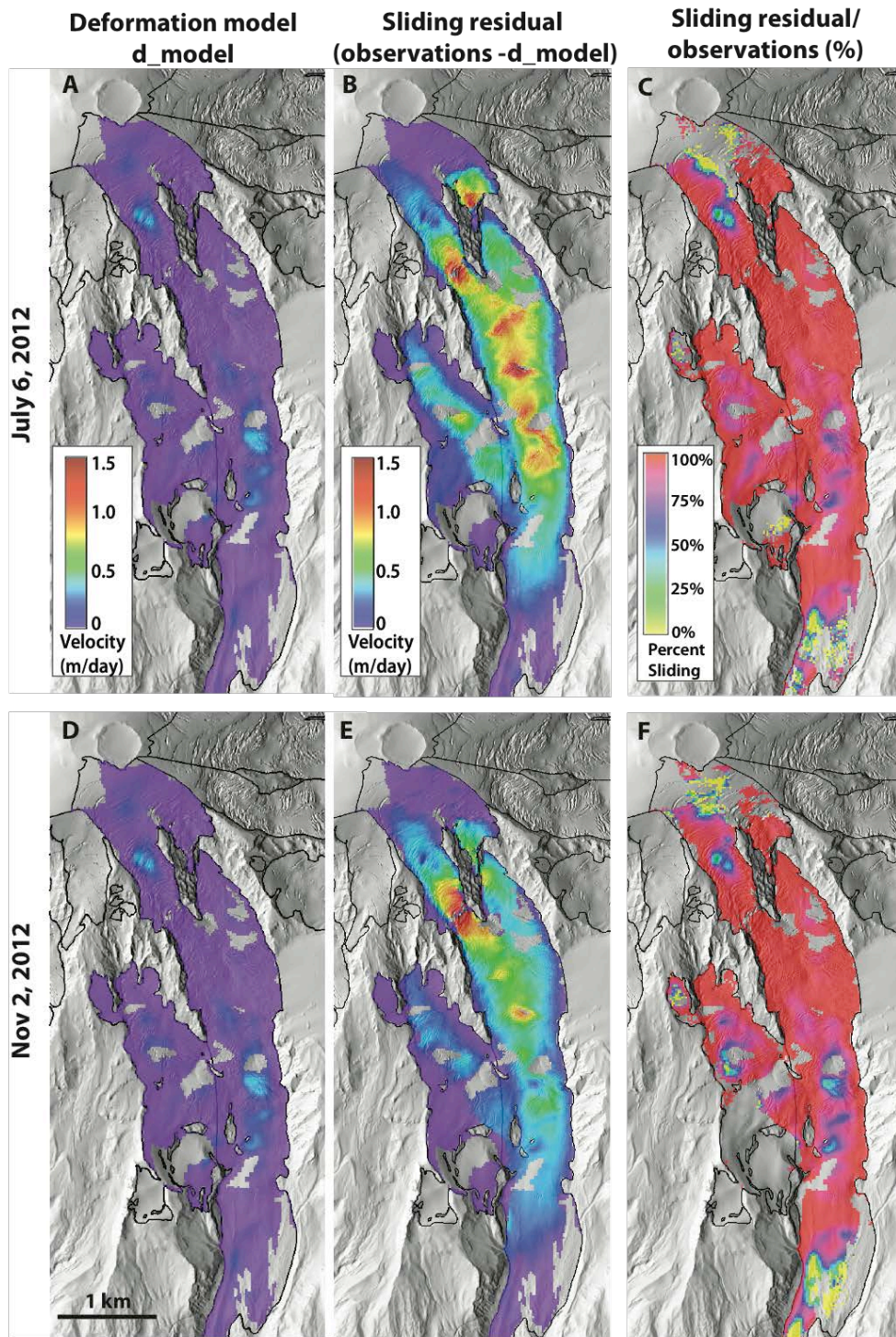
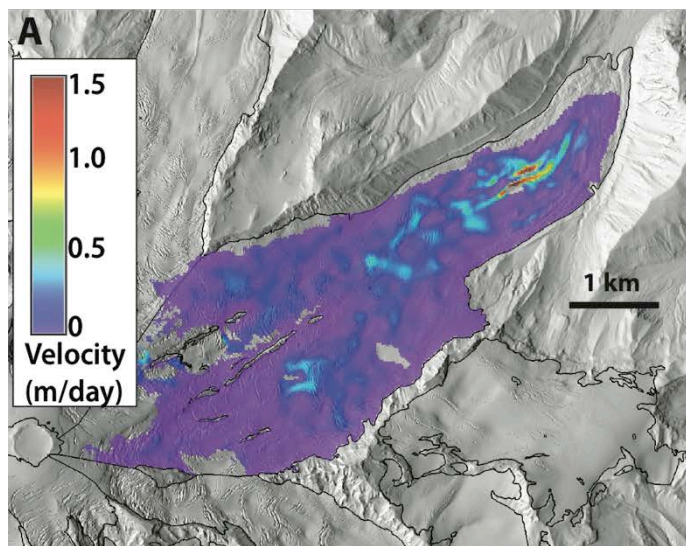
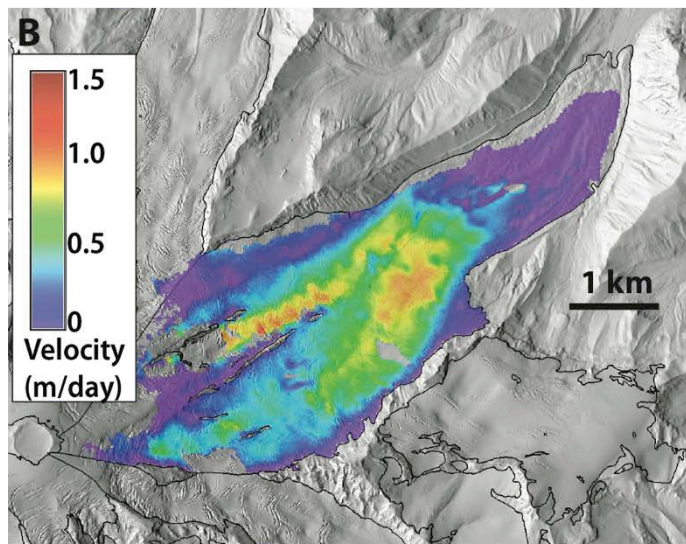


Figure 10

Deformation model
d_model



Sliding residual
(observations - d_model)



Sliding residual/
observations (%)

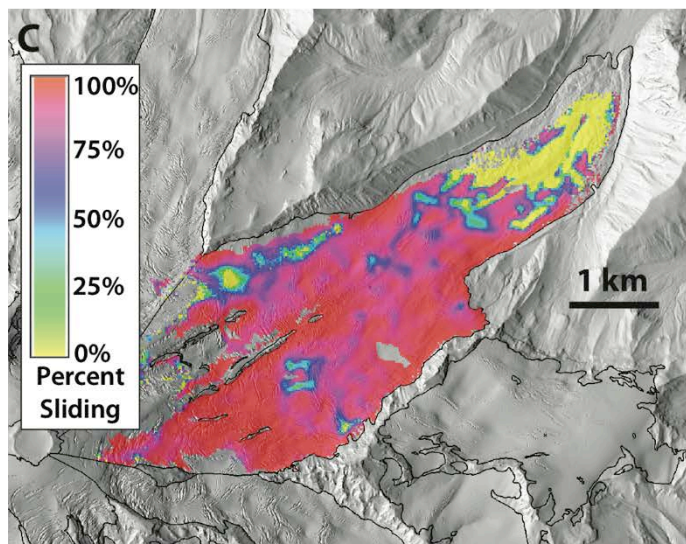


Figure 11

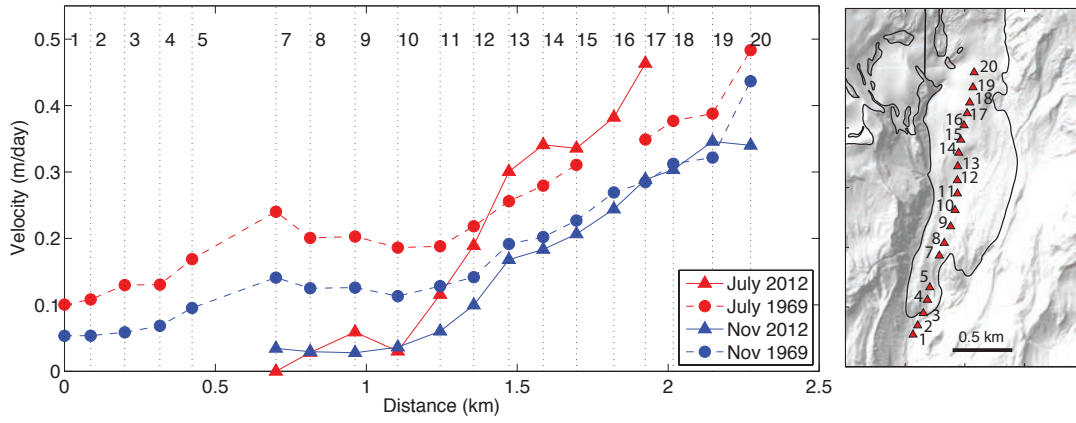


Figure A1

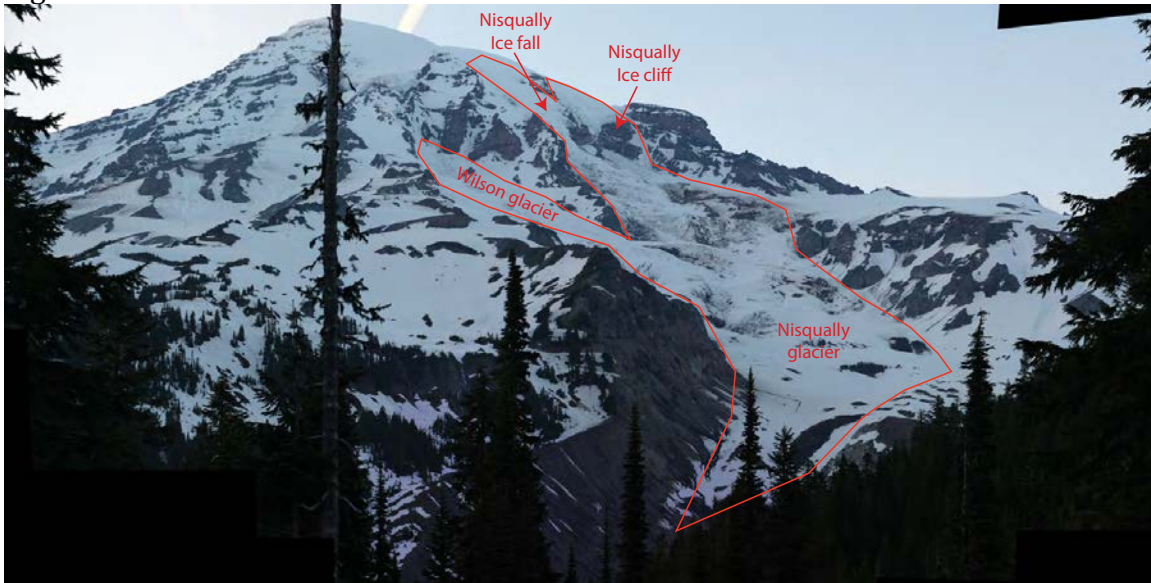


Figure A2

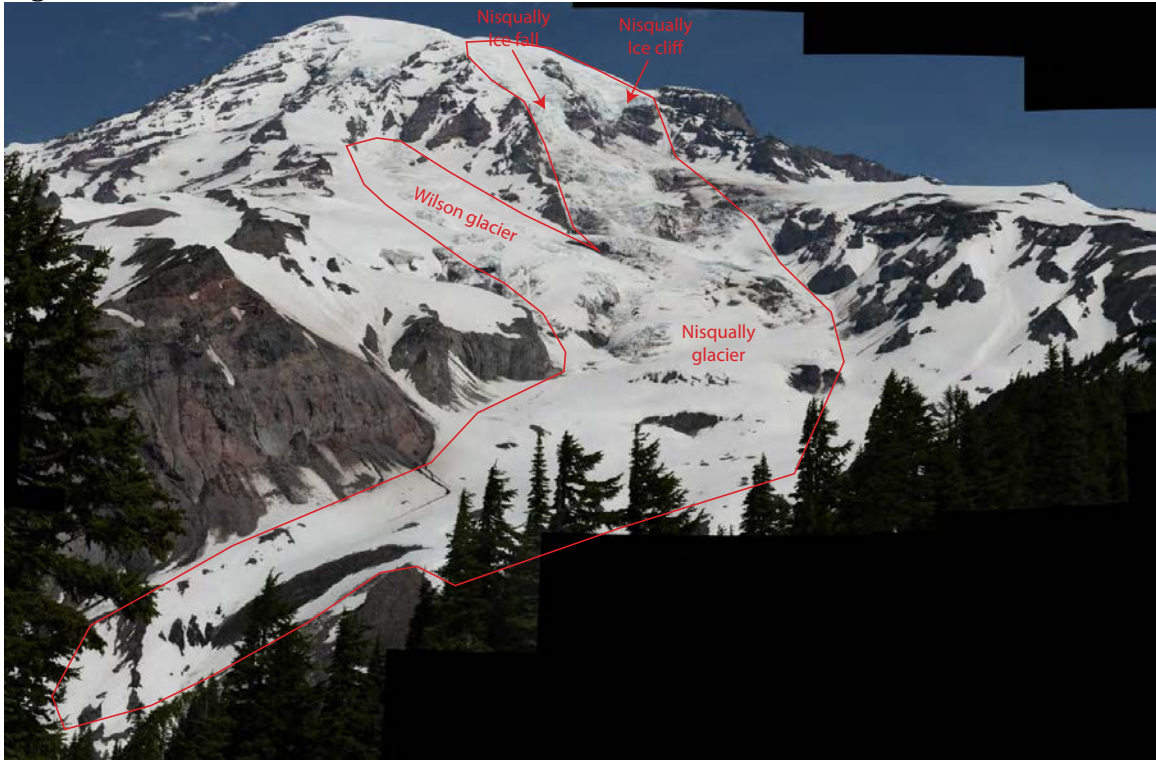


Figure A3



Figure A4

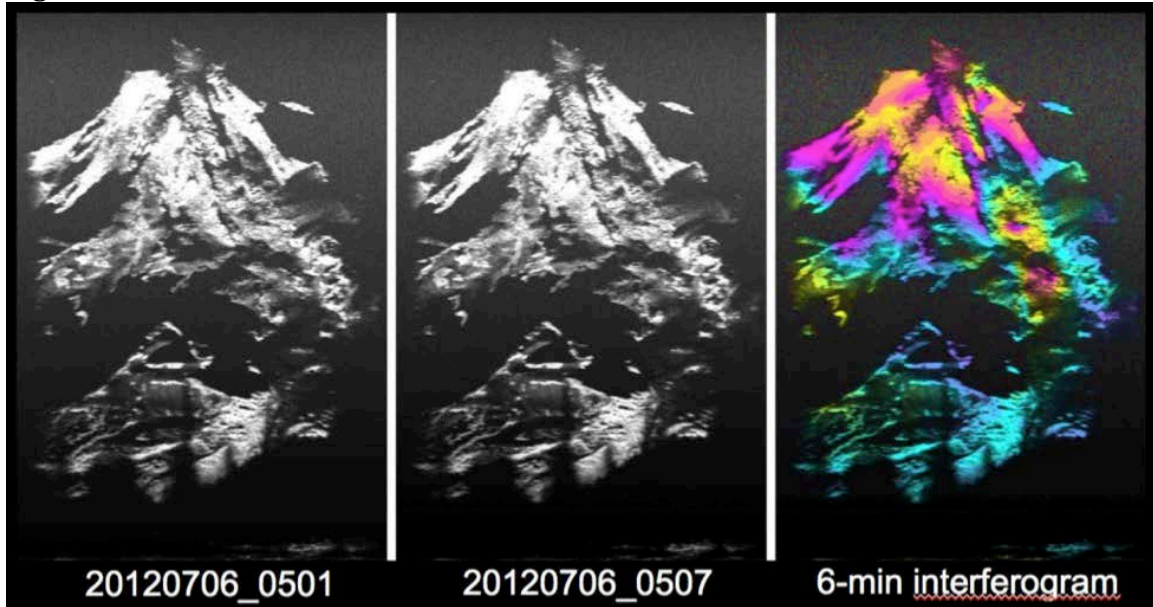


Figure A5

